Modulation of Nanoparticle Uptake, Intracellular Distribution, and Retention with Docetaxel to Enhance Radiotherapy

by

Aaron Bannister

B.Sc., University of Victoria, 2017

A Thesis Submitted in Partial Fulfillment

of the Requirements for the Degree of

MASTER OF SCIENCE

in the Department of Physics and Astronomy

University of Victoria

We acknowledge with respect the Lekwungen peoples on whose traditional territory the university stands and the Songhees, Esquimalt and WSÁNEĆ peoples whose historical relationships with the land continue to this day.

Supervisory Committee

Modulation of Nanoparticle Uptake, Intracellular Distribution, and Retention with Docetaxel to Enhance Radiotherapy

by

Aaron Bannister

B.Sc., University of Victoria, 2017

Supervisory Committee

Dr. Devika Chithrani, (Department of Physics and Astronomy)

Supervisor

Dr. Isabelle Gagne, (Department of Physics and Astronomy)

Departmental Member

Dr. Cornelia Hoehr, (Department of Physics and Astronomy)

Departmental Member

Abstract

OBJECTIVE:

One of the major issues in current radiotherapy (RT) is the normal tissue toxicity. A smart combination of agents within the tumor would allow lowering the RT dose required while minimizing the damage to healthy tissue surrounding the tumor. We chose gold nanoparticles (GNPs) and docetaxel (DTX) as our choice of two radiosensitizing agents. They have a different mechanism of action which could lead to synergistic effect. Our first goal was to assess the variation in GNP uptake, distribution, and retention in the presence of DTX. Our second goal was to assess the therapeutic results of the triple combination, RT/GNPs/DTX.

METHODS:

We used HeLa and MDA-MB-231 cells for our study. Cells were incubated with GNPs (0.2nM) in the absence and presence of DTX (50nM) for 24 hrs for determination of uptake, distribution, and retention of NPs. For RT experiment, treated cells were given a 2 Gy dose of 6 MV photons using a linear accelerator.

RESULTS:

Concurrent treatment of DTX and GNPs resulted in over 85% retention of GNPs in tumor cells. DTX treatment also forced GNPs to be closer to the most important target, the nucleus, resulting in a significant decrease in cell survival with the triple combination of RT, GNPs, and DTX vs. RT plus DTX alone. Our experimental therapeutics results are supported by Monte Carlo simulations.

CONCLUSION:

The ability to not only trap GNPs at clinically feasible doses but also to retain them within the cells could lead to meaningful fractionated treatments in future combined cancer therapy. Furthermore, the suggested triple combination of RT/GNPs/DTX may allow lowering the RT dose to spare surrounding healthy tissue.

ADVANCES IN KNOWLEDGE: This is the first study to show intracellular GNP transport disruption by DTX, and its advantage in radiosensitization.

KEYWORDS: Gold nanoparticles, Docetaxel, endocytosis, exocytosis, microtubules, tumor cells, cell cycle

Table of Contents

List of Tables

List of Figures

Symbols & Abbreviations

DLS – Dynamic Light Scattering
DNA – Deoxyribonucleic acid
DSB – Double strand break
EPR – Enhanced permeability and retention
FBS – Fetal bovine serum
fcc – face-centred cubic lattice
FS – Field Size
GNP – Gold nanoparticle
ICP-MS – Inductively coupled plasma – Mass spectroscopy
LINAC – Linear Accelerator
LSPR – Local Surface Plasmon Resonance
MU – Monitor Unit (measure of machine output from a clinical accelerator for radiation therapy)
NP – Nanoparticle
PEG – Polyethylene Glycol
PBS - Phosphate Buffered Saline
RGD – Arginine-Glycine-Aspartic acid-containing peptide
RNA- Ribonucleic acid
ROS – Reactive Oxygen Species
RME – Receptor-mediated endocytosis
SF – Survival Fraction
SEM – Scanning electron microscopy
UV-VIS – Ultraviolet-Visible

Acknowledgements

I would like to thank Dr. Wonmo Sung and Dr. Jan Schuemann at Harvard Medical School for performing Monte Carlo simulations based on our uptake data. Thanks also go to Monica Mesa and Dr Perry Howard of UVic Biochemistry and Microbiology for sharing their expertise in flow cytometry, as well as Dr. Robert Chow for training in confocal microscopy techniques. Finally, thanks to Kyle Bromma and Leah Cicon, for always being willing to lend a hand for cell counting.

Dedication

I would like to thank Devika Chithrani for giving me a chance and never letting me settle for less than my best.

Thank you, Tristan my love, for helping me push through the tough times and for also helping me give myself permission to rest when I needed it.

Thank you to Alyssa, for helping me cultivate the skills to keep myself from burning out.

.

Chapter 1: Introduction

1.1 Introduction to Cancer Treatment Strategies

1.1.1 The Basics of Cancer

Cancer is a collection of diseases that feature the unregulated division of cells. Much of the unregulated division is due to mutations that disable the regulatory genes that halt cell division in response to genetic defect or that cause apoptosis (programmed cellular death) in damaged cells. Unable to restrict growth or prevent damaged cells from dividing, the cells undergo unregulated proliferation. They collect mutations rapidly and eventually evolve to invade tissues and metastasize into surrounding tissues. Because they arise from a person's own cells, they have markers that allow them to invade the immune system and grow without contest and out-compete healthy cells for nutrients and blood supply, eventually killing the patient.[1]

1.1.2 The Primary Challenge in Cancer Treatment

Cancer treatment is often difficult due to the low "contrast" between the healthy normal cells and the cancer cells. Because cancers are derived from a patient's own healthy cells, they often have only minor changes in the Major Histocompatibility Complex, the set of cell surface markers that identify an organism's own cells to its immune system. Further, they are still human cells and share most functions with healthy cells. This means that unlike in the case of antibiotics and antifungals, most drugs that affect cancer will also damage the patient.[2] Successful cancer treatment lies in exploiting the subtle differences found in the damaged cells.

1.1.3 Targeting Strategies for Cancer Treatment

Cancer therapy is usually targeted in either a geometric or functional fashion. Functionally targeted treatments affect a property or function inherent to the cancer cells that is either different from normal cells or expressed to a different degree. Most chemotherapies are functional in nature, with targeting of cell division being very common as cancers generally divide much faster than healthy tissues. They are usually administered systemically i.e. to the entire body, intravenously or orally. Mechanistic treatments have the advantage of being able to affect tumours throughout the patient including undetectable metastases, but often cause toxicity in normal organs and rapidly-dividing healthy tissues.[3] Geometrically targeted therapies rely on macroscopic properties of cancerous tissue, generally the location or geometry. These treatments include surgical intervention and radiotherapy. They can be targeted locally to spare normal tissue from damage, e.g. by not cutting normal tissue, but are unable to treat metastases that are undetectable or outside of the targeted region.[4]

1.1.4 Measuring Success: The Therapeutic Ratio

The ideal goal of cancer treatment is 100% tumour control, i.e. to halt all division of cancerous tissues by cell death or sufficient damage. Unfortunately, due to the difficulties encountered in targeting cancer therapies, this is often not practically possible as the collateral damage to the patient would cause death or unacceptable side-effects. The therapeutic index or ratio are tools used to assess the balance between tumor control and patient quality of life. Essentially, the therapeutic index is a measurement of the contrast a treatment is able to “see” between normal and cancerous cells.

In chemotherapy, the therapeutic index is the ratio between the *maximum tolerated dose* (MTD) and the *effective dose* (ED) of a drug. The MTD is the highest dose of a drug that can be administered without unacceptable complications or side effects, while the ED is the dose at which the drug has the desired pharmacological effect.[5] For radiotherapy, the therapeutic ratio is the ratio of tumor control probability and the probability of normal tissue damage or complication. In practice, the normal tissue damage considers not only acute side effects, but also long-term damage and patient quality of life.[4] For a given treatment, physicians set the upper tolerance for complications, which limits the achievable tumor response. Much of the research in cancer therapy is aimed at finding treatments or combinations of treatments that increase the therapeutic index or ratio.

1.1.5 Combining Strategies for Improved Outcomes

A common strategy in chemotherapy is to combine drugs with non-overlapping mechanisms and profiles of side effects. In this way, the damage to the cancer is maximized through the combined effects of the drugs while the side effects are “spread out” over different organ systems such that none receives serious enough damage to incur devastating side effects. This also prevents anti-drug resistance from evolving in the tumour.[3]

Another strategy is combining the local and systemic effects of radiotherapy and chemotherapy treatments. A radiosensitizer is a drug that has effects that make a cell more vulnerable to radiation; sometimes in addition to other therapeutic properties. Several chemotherapy drugs, such as cisplatin, are currently used as radiosensitizers.[6] Radiosensitization mechanisms vary from directly amplifying the radiation dose or creating additional reactive oxygen species to making the cell ignore DNA damage.[7] This improves the treatment ratio by exploiting the synergistic effect of radiosensitizers to deal amplified damage only within the irradiated volume.[4]

However, combined and simultaneous normal-tissue toxicity in such treatments is a major barrier to the effectiveness of combined chemotherapy and radiotherapy. Due to possible microscopic tumour invasion of surrounding tissue, the irradiated volume in RT necessarily will include healthy tissue in addition to the tumour.[8] Systemic radiosensitizers will also radiosensitize normal tissues, which can lead to unacceptable toxicity. In **Figure 1**, this would appear as both curves shifting to the left.[4] The ability to selectively deliver radiosensitizers to cancer cells would protect normal tissues and greatly increase the therapeutic ratio. This would appear in as only the tumour control curve shifting left. Recently, nanoparticle systems have been developed, which deliver drugs to cancer cells via active targeting rather than passive diffusion. More on this topic is discussed in 1.4.

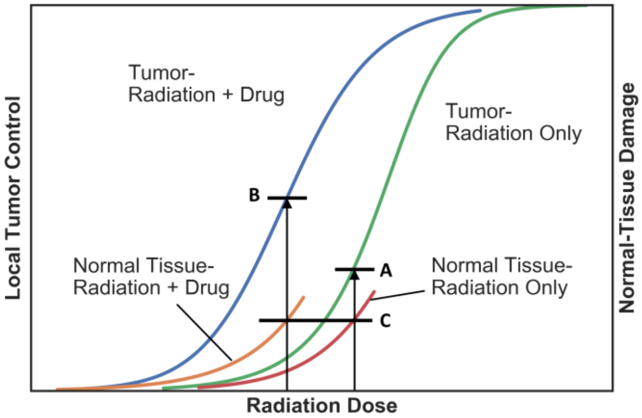

Figure 1: The therapeutic ratio.

Therapeutic ratio is defined as the ratio of the local tumor control probability (A) at the radiation dose that has the maximally allowable probability of normal tissue complication (C). Addition of a drug may reduce the allowable radiation dose but increase the effectiveness of that level of radiation (B). Reproduced from Radiobiology for the Radiologist, Seventh Edition. [4]

1.2 Biological Considerations – The Eukaryotic Cell

In this section, we give a review of important structures in the eukaryotic cell and their relevant characteristics to this study.

1.2.1 The Nucleus: DNA Damage and Repair

The genetic material for every cell is found within the cell's nucleus. This genetic material, DNA, contains the genes that guide the function of the cells. When these cells divide, it is vital that the genetic material in the nucleus replicates itself accurately. When DNA is damaged or DNA-replication errors occur in a healthy system, monitoring proteins pause the cell cycle until the damage can be repaired or apoptosis is initiated.[9]

Damage can occur in double helix DNA strands due to breaks in the strands. Single-strand breaks are readily repaired by copying the undamaged section available in the other strand of the helix.[10] *Double-strand breaks* (DSBs) are the most damaging to the cell and, not properly repaired, can lead to cell death. Their two main repair pathways *homologous recombination* (HR) and *non-homologous end joining* (NHEJ). Since the cell has two copies of every chromosome, the corresponding region of an undamaged sister chromosome can be used as a template to rejoin severed strands. This typically occurs in the S or G2 phases while the DNA is being replicated or prepared for cell division. NHEJ does not require a template and can occur in any phase of the cell cycle. The accuracy of NHEJ depends on there being few DSBs in close proximity to each other. When there are many DSBs, the wrong ends can be joined. This can result in fragmented or looped chromosomes, which can get lost during mitosis or prevent mitosis from occurring properly in an event known as *mitotic catastrophe* (MC).[4]

1.2.2 The Cell Membrane: Endo/Exo-cytosis and Integrins

The plasma membrane of a eukaryotic cell closes off the cell from the surrounding environment and manages the internal environment, which allows the creation and maintenance of concentration gradients. In order to function, the cell actively and passively manages transport of substances across this membrane, such as by importing sugars or expelling waste. The cell will also import amino acids, nucleotides, and other molecules it needs in order to function. Many of these proteins are either embedded within or attached to the plasma membrane and are involved in processes such as cross-membrane transport, signal reception, or cytoskeleton attachment. The membrane surrounds cytoplasm, an aqueous solution of dissolved and colloidal organic molecules and proteins in which the organelles of the cell situate.

Endocytosis is a process by which the cell membrane invaginates and buds into the cell, creating a vesicle called an endosome. The endosome contains both membrane proteins and extracellular fluid. The most common form of endocytosis is receptor-mediated endocytosis, where the cell absorbs metabolites or particles. Receptors on the cell surface bind with specific molecules in the extracellular environment. They are collected together on the cell membrane by clathrin, which forms a protein “cage” that pulls the cell membrane into a pit.[11] This pit then buds off the cell surface, forming an vesicle. Only the receptor-bound substances can enter the vesicle. The vesicle then fuses with an endosome for initial processing and sorting. Many receptor proteins are quickly recycled back to the cell surface, and the endosome contents are sorted into various processing paths such as into lysosomes for breakdown of large proteins into component amino acids.[12]

Exocytosis is the reverse process, where a vesicle containing for example waste products from lysosome processing merges with the cell membrane and expels its contents into the extracellular fluid.

Integrins are a family of membrane proteins that principally interact with the extracellular matrix (ECM), a three-dimensional network of collagen and other macromolecules that acts to adhere cells and tissues and facilitates cell-to-cell communication. The integrins are used to bind the cell to the ECM to hold it in place, and during cell migration they are rapidly endocytosed and recycled to different parts of the cell surface up to attach to new parts of the ECM.[12] Integrins are often overexpressed in cancer cells, which makes them exploitable for use for targeted therapies. Various viruses are known to target integrin for transport into the cell, and in this this study this was used to facilitate gold nanoparticle uptake as discussed in section 1.4.[13]

1.2.3 Microtubules and Intracellular Transport

Microtubules (MTs) are a major component of the cytoskeleton of the cell, a regulated amorphous latticework of fibrous protein polymers that facilitate cell morphology and motility as well as provide a framework for the localization of organelles and transport of cargoes within the cell. MTs are composed of α- and β-tubulin proteins, which form dimers that float free in the cytoplasm. Microtubule formation is nucleated in the microtubule organizing centre (MTOC), usually located near the nucleus of the cell (See **Figure 8a**(i), pg. 22). Tubulin dimers are recruited to link in end-to-end chains called protofilaments, which then 'zip' together to form hollow microtubules (**Figure 2**). The MTs are polarized, with a negatively charged end (-) at the nucleation site and polymerization occurring at the

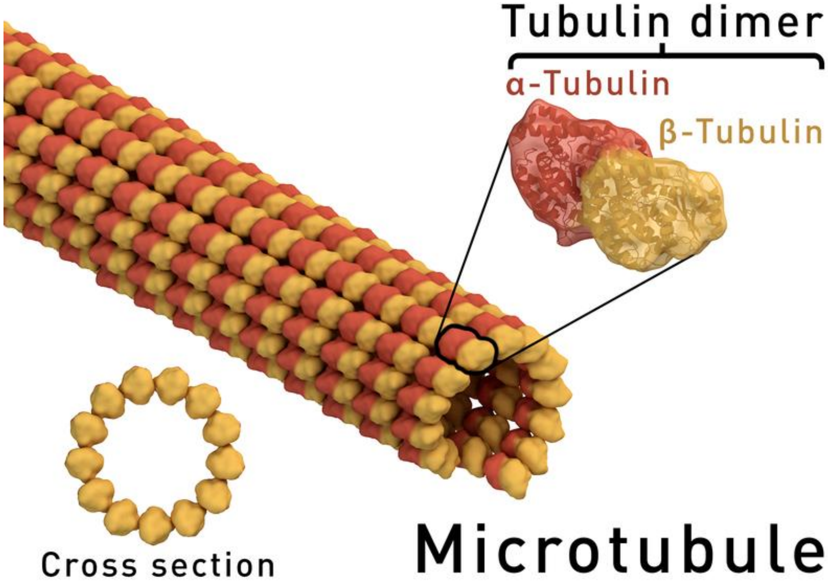

Figure 2: Schematic of a microtubule.
Image credit: Thomas Splettstoesser (www.scistyle.com)
(https://commons.wikimedia.org/wiki/File:Microtubule_structure.png),
https://creativecommons.org/licenses/by-sa/4.0/legalcode

positive end (+). The polymerization process is reversible and most MTs exist in dynamic instability, with the (+) end alternately growing or shrinking depending on its local environment.

Many cargoes such as endosomes are transported throughout the cell by motor proteins that ratchet along the MTs, directed to one of the polar ends. MTs are also critical for cell division, as they compose the mitotic spindle that allows for DNA segregation into daughter cells. This is discussed further in Section 1.5.1.

1.2.4 The Cell Cycle

The eukaryotic cell cycle can be divided into four major phases; G1, S, G2, and M. The genetic information is duplicated during the synthesis (S) phase and the cell divides into two daughter cells during mitosis (M). S phase and mitosis are separated by Gap phases, G1 and G2.[2]

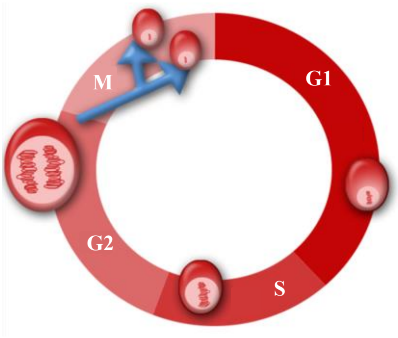

Figure 3: Schematic diagram of the cell cycle. Image credit: Tristan Bannister

Progress through the cell cycle is regulated by several checkpoints, which monitor the state of the cell and its extracellular environment as it prepares for division. These checkpoints are driven by a protein family called cyclin-dependent kinases (CDKs). CDKs are a collection of signaling proteins whose action varies through the cell cycle. The specificity of the CDKs is dependent on which of another class of proteins (called cyclins) is bound to it. The concentration of various cyclins changes with the cell cycle allowing the behavior of the CDKs to change as well.[2] For example, CDK2 interacts with D-cyclins during the G1 phase and Cyclin A during the S phase.[14]

1.3 Radiotherapy

1.3.1 Radiotherapy in Cancer Treatment

Roughlyfsdxc half of all cancer will receive radiotherapy as part of their treatment process, according to current best practices.[15] It is suitable for long-term control of a variety of cancers including head and neck, lung, and skin cancers, as well as palliative care.

In radiotherapy, damage is done via a high dose of ionizing radiation delivered to the tumor site. X-ray photons, electrons, and protons are common sources of radiation for the purposes of treatment.[16] Ionization of molecules in the cells is caused directly by charged particles (electron or proton therapy) or indirectly by secondary electrons ejected by these ionizations (photon or electron therapy). The reactive molecules produced by this radiation go on to damage important structures in the cells, eventually leading to cell death.[8]

In this thesis, only external beam x-ray radiotherapy (EBRT) will be discussed, as this is the most commonly used for treatment. The main challenge in EBRT is that the beam cannot be blocked within the patient. It will damage both normal and cancerous tissues along the entire beam.

1.3.2 Radiotherapy physics

The use of x-rays for the treatment of cancer has been common in clinical applications since their discovery in 1895. It is used for the purposes of curative treatment, but also for palliation. The type of radiation used in cancer therapy interacts with the materials as it passes through. Because it forms charged particles, or ions, as it passes through the material, it is called ionizing radiation.[17] It also deposits energy, which kills the cancer cells.

To deliver EBRT, Linear accelerators (Linacs) are used to generate x-ray photons. These machines accelerate electrons, then collide them with a heavy metal target to produce the x-ray photons. In a clinical setting, mega-voltage energy beams are usually referred to by their maximum energy, corresponding to energy of the impacting electrons. For example, a beam of 6MeV electrons impacting a target would produce a 6 mega-voltage peak (MV) photon beam. These beams can be applied to a number of treatment or imaging modalities. One example is Volumetric Modulated Arc Therapy (VMAT), a high-precision radiotherapy that combines precise collimation and a moving gantry to “paint” a tumour volume with x-ray beams from many directions. This allows for a high dose region that closely conforms to the tumour geometry while spreading out collateral dose and avoiding beaming through critical structures.[18]

1.3.3 Radiation Interactions with Tissue

Human tissues are composed of millions of cells. Cells are primarily (70%) made of water, with the balance being made up of dissolved salts and biomolecules such as DNA and proteins. Ionizing radiation does not interact with molecules as a whole, but rather the charged particles which make up the atoms that compose these molecules. It is these charged particles and their subsequent effects that are important when discussing the damage caused to tissues by radiation.

An atom consists of a cloud of negatively charged elections (e-), bound to a positively charged nucleus. An atom with atomic number Z will have Z positively charged protons (p) and N neutral neutrons (n), with its atomic mass A being the sum of Z and N. For example, Carbon-12 (the most abundant form of Carbon) has $A = 12$, with $Z = 6$ protons and $N = 6$ neutrons. Most atoms are found in an electrically neutral state, with the same number of electrons as protons.

Electrons within atoms are arranged in shells of decreasing energy with increasing average distance from the nucleus. Those in inner shells experience a greater attractive force from the nucleus, while those toward the outside are screened from some of the nucleus’ charge by those inner shells. The binding energy of an electron therefore depends both on the atomic number and the electron’s shell, given approximately by the Moseley rule:

$$W = -13.6\,\text{eV}\,\frac{(Z-\sigma)^2}{n^2}$$

Where W is the binding energy expressed in electron volts (eV), n is the principal quantum number of the electron's shell, and σ is an empirically derived screening correction which depends on both Z and n.

X-rays deposit energy in tissue in a stochastic manner, with the type of interaction and its location depending on the interacting material and the X-ray energy. An x-ray photon can interact with either the electrons or the nucleus of an atom. Electrons can interact with X-rays via the photoelectric effect or scattering, while nuclei can cause either the photonuclear effect or pair production. Over clinically relevant energies ($20\,\text{keV}$ - $15\,\text{MeV}$), different interactions become dominant for different energies and materials (see **Figure 4**).

The probability of interaction between an x-ray and an atom in a homogeneous medium is constant for each encounter, thus the probability of an x-ray traveling a given distance within the medium falls off exponentially with distance. The decay constant of this exponential is the linear attenuation coefficient μ, which depends on the photon energy and the atomic number of the absorber. μ can be expressed as the sum of linear attenuation contributions from the various interaction types:

$$\mu = \tau + \sigma + \kappa + \sigma_R + \sigma_{PN}$$

Where τ represents photoelectric interaction, κ is pair production, σ_{PN} is photonuclear interaction, and σ and σ_R are Compton and Rayleigh scattering respectively. Attenuation is often scaled by density (ρ) to produce the mass attenuation coefficient (μ/ρ) to more easily model mixed or inhomogeneous materials.

Most of these interactions will deposit energy at the point of interaction in the form of an ejected electron. The energy deposited per unit mass is measured in Gray (Gy), equivalent to one Joule per kilogram. For tissue, this corresponds to roughly 10^5 ionizations.[8]

1.3.3.1 The Photoelectric Effect

In a photoelectric interaction, a tightly bound inner shell electron is ejected by absorbing a photon. This electron has a kinetic energy equal to the incoming photon energy less its binding energy. The vacancy left is quickly filled by an outer-shell electron, releasing a characteristic x-ray with energy equal to the binding energy difference between the electron

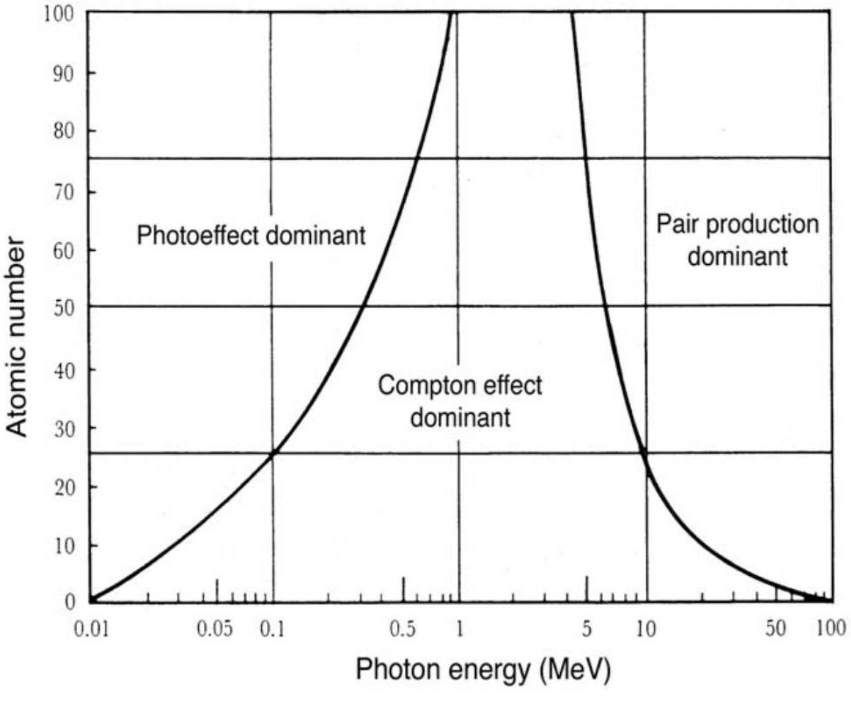

Figure 4: Regions of relative predominance of the three main forms of photon interaction with matter. Adapted from Podgorsak, E.B., Radiation Oncology Physics: A Handbook for Teachers and Students. 2005, Vienna: International Atomic Energy Agency.

shells. This interaction is dominant when the x-rays have energy comparable to the binding energy.

The energy of the electron filling the vacant inner shell may also be transferred to an electron in a shell further out, ejecting it as an Auger electron. The new vacancy is also quickly filled, and this process may be repeated. For high-Z materials with many electrons such as iodine, this "Auger cascade" may eject as many as 15 electrons with various energies mixed with characteristic x-rays.

1.3.3.2 Compton and Rayleigh scattering

In a scattering process, When an X-ray photon scatters, it changes direction and loses some energy. For low-energy photons and inner shell electrons, a photon can scatter off of the electron without ironizing the atom. The photon changes direction while losing a negligible amount of energy, and the atom as a whole picks up a slight momentum in recoil. This is Rayleigh or incoherent scattering.

When the binding energy of an electron is negligible compared to the photon energy, the photon may Compton scatter off the electron as if it is unbound. The photon is deflected at a significantly reduced energy and the electron is ejected from the atom. The scattered x-ray may continue on to cause another ionization. This process is dominant between about $0.5 - 5\ \mathrm{MeV}$, depending on the atomic number.

1.3.3.3 Pair production

At photon energies above 1.022 MeV, or twice the mass energy of an electron, photons may scatter off the nucleus of an atom and produce an electron-positron pair. The nucleus picks up a small amount of recoil to conserve momentum while any additional photon energy is transferred to the electron and positron as kinetic energy. The positron may travel some distance before annihilating with another electron, producing two new 511keV photons. This process becomes more probable with higher Z and photon energy.

1.3.3.4 The Photonuclear effect

At energies beyond a few MeV, an X-ray photon can directly eject a proton, neutron, or alpha particle from a nucleus in a process analogous to the photoelectric effect. The ejected particle can produce further ionizations or interact with other nuclei to create unstable isotopes. This is a very rare interaction and typically is relevant to clinical beam energies of 10MV or higher. In this thesis, only 6MV photon beams were used, so this effect is not considered further.

1.3.3.5 Beam Changes in Tissue

In each of the energy depositing processes outlined above, the end product is a fast-moving electron often accompanied by a photon of lower energy than the inciting one. As a megavoltage x-ray beam passes through tissue, it becomes contaminated by low energy photons. These photons do not travel very far in tissue but are produced along the beam path so are present within the entire irradiated volume of the patient.

1.3.4 Radiobiology

The primary goal of radiotherapy is to cause enough damage to a cancer cell’s DNA that is dies or can no longer divide. In a typical clinical scenario, the radiation beam is far wider than the cell and the dose is distributed randomly throughout. This will damage or destroy many biomolecules such as proteins and RNA, but these are present in many copies and are typically rapidly replenished, thus limiting the biological effect. DNA is present in only two copies in each cell and is infrequently replicated, thus it serves as a critical point of failure for cell survival.

While it is possible for the radiation interactions discussed above to damage DNA directly through ionization, this is relatively unlikely as DNA only makes up a small fraction of a cell's mass. Most DNA damage comes about due to ionization via the secondary elections produced by x-ray interactions or by reactive species called "free radicals" that are produced as the electrons ionize other molecules in the cell. As these secondary electrons move, they lose energy by colliding with molecules and ionizing them in turn. They slow down, ionizations become more frequent, and the end of an electron's track typically consists of a small cluster of ionizations in a space about the width of a single DNA strand. The linear energy transfer (or number of ionizations per distance traveled) is important when considering radiation damage as a cluster of ionizations near a DNA strand is more likely to cause a double strand break.

In radiotherapy research, cell death is defined as the loss of reproductive capacity. A radiation-damaged cell may be able to continue dividing a few times before critical DNA damage causes senescence or death. To account for this, radiation survival is typically measured using a clonogenic or colony-formation assay, where individual irradiated cells are cultured for several days before counting the number of colonies larger than a threshold number of cells.

1.4 Gold nanoparticles as radiosensitizers

High-Z materials have long been used in X-ray imaging due to their high photoelectric effect cross sections. For example, iodine (Z=53) is routinely used to create contrast in blood vessels for computed tomography (CT) scans. The absorption coefficient for the photoelectric effect scales roughly as Z^3, so materials like gold ($Z = 79$) can have a vastly higher absorption than tissue ($Z \sim 7.5$). For kilovoltage X-rays, this also allows for dose enhancement. X-rays will preferentially interact with the high-Z material and produce short-range secondary electrons. For example, introducing an iodine-based contrast agent intravenously[19] or intratumorally[20] showed significant radiosensitization in animal models along with *in vitro* use of iododeoxyuridine, an iodine-containing DNA-binding drug[21].

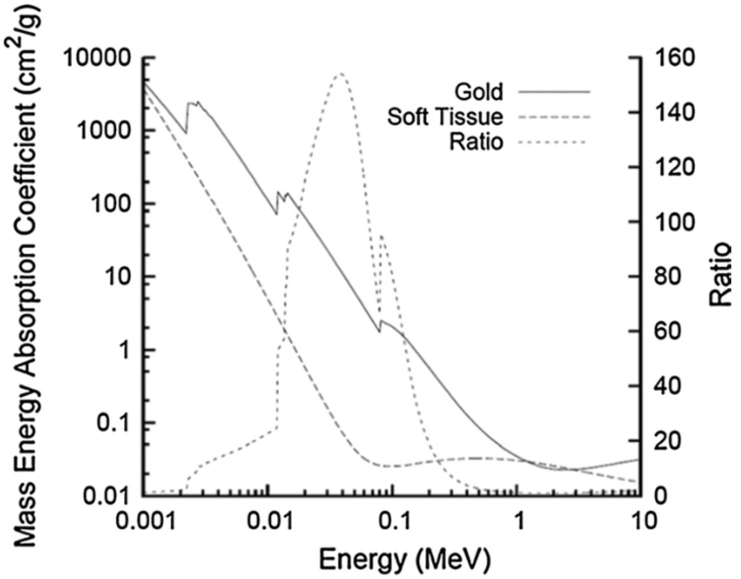

Figure 5: Photon mass energy absorption coefficients of soft tissue and gold.
The ratio of mass energy absorption coefficients is shown as a function of photon energy. Reprinted from Rosa, 2019 with Creative Commons licence: https://creativecommons.org/licenses/by/4.0/legalcode.

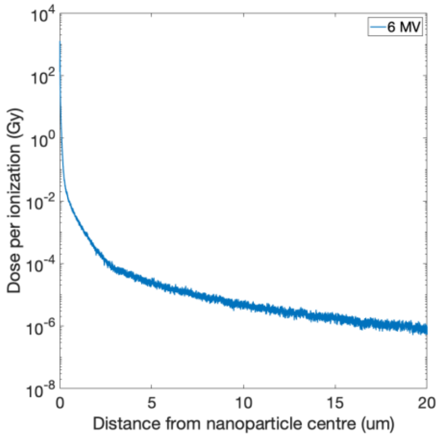

Figure 6: Dose profile near a 15nm GNP irradiated by a 6MV photon beam. Adapted from Sung et al (2017) with permission.

More recently, nanoparticle (NP) systems incorporating heavy elements have been investigated as radiosensitizers.[22, 23] NPs are particles between 1-1000 nanometres, and often have different properties than those seen in bulk material of the same composition. Nanoparticles can be tailored to therapeutic goals by modifying their size, shape, and surface properties.[24-26] They can also act as carriers for drugs and other molecules.[27, 28] Gold nanoparticles (GNPs) are particularly promising due to their simple surface chemistry, biocompatibility, and ease of manufacture.[24, 29] Gold nanoparticles first showed promise in a mice tumor graft study by Hainfeld *et al*. Using 1.9nm GNPs and 30Gy of 250 kilovoltage-peak (kVp) X-rays, he achieved 86% long-term survival versus 20% with X-rays alone. He also observed preferential uptake of the nanoparticles by the tumors compared to normal tissue.[30]

1.4.1 Radiosensitization Mechanisms of Gold Nanoparticles

The predominant radiosensitizing effect of GNPs is the creation of secondary electrons. Due to its higher density and atomic number than tissue, gold has a much higher absorption cross-section between 10 and 200 keV as seen in **Figure 5**. Within this energy range, gold primarily interacts via the photoelectric effect. This produces a relatively low-energy, high-LET electron.[16] The resulting inner shell vacancy can initiate an Auger cascade, spreading out much of the remaining energy balance of the interaction into more low-energy electrons.[31] The net effect is a spray of short-range electrons that can cause many ionizations as they slow in the surrounding medium. The dose profile for GNPs is highly peaked and microscopic in extent (**Figure 6**).[32] For this reason, GNPs must be present in high concentration or localized very close to the nucleus in order to cause excess DNA DSBs.[32]

GNPs can also cause damage via the creation of reactive oxygen species (ROS) such as superoxide (O_2^-) and hydrogen peroxide, though the exact mechanism is not yet known. These species can do damage directly to DNA or other biomolecules or cause oxidative stress which can lead to apoptosis or necrosis (unregulated cell death due to stress).[33]

While the relative dose enhancement and range of secondary electrons is higher when using a kilovoltage x-ray beam, meaningful enhancement can still be achieved with megavoltage beams due to contamination of the beam by lower-energy scattered photons and secondary electrons produced as it passes through tissue.[34] This has been verified by Chithrani *et al*, who found a dose enhancement factor of 1.17 for 6MV radiation vs. 1.66 at 105kVp. This means that deep-seated tumours that cannot be effectively treated with shallowly-penetrating kilovoltage beams could still benefit from GNP-enhanced radiotherapy.

1.4.2 Functionalization and Uptake of GNPs

1.4.2.1 Enhanced Permeation and Retention (EPR) effect

Nanoparticles for cancer therapy are generally administered intravenously and are passively targeted to tumours by the enhanced permeation and retention (EPR) or "leaky vasculature" effect. Like other tissues, tumours can recruit vascular endothelial cells to line new blood vessels. However, they generally grow too fast to maintain a complete lining in their vasculature. Most nanoparticles, due to their relatively large size compared to most biomolecules, are unable to diffuse through normal blood vessel linings. The gaps present in tumors allow for rapid accumulation of nanoparticles in the tumor tissue and thus produce a passive selective targeting effect. Further, lack of lymphatic circulation in tumours can allow for retention of the nanoparticles for much longer than in normal tissues.[35]

Bare GNPs, like many nanoparticles, have poor circulation lifetimes when administered intravenously. They attract a layer of plasma proteins to their surface, which can enhance uptake into cells but also causes immune cells to clear them from the bloodstream. Poly(ethylene glycol) can be thiol-bonded to the GNP surface; this hydrophilic polymer shields the GNP from the plasma proteins and allows it to evade the immune system.[36] However, it also reduces endocytosis in cancer cells. To combat this, we use a polypeptide containing an integrin binding domain Arginine-Glycine-Aspartic Acid (RGD) with a cysteine terminus that can thiol-bond to the gold. As integrins are overexpressed on the surface of many cancers, this provides an avenue for active targeting to cause nanoparticles to enter cancer cells.[37]

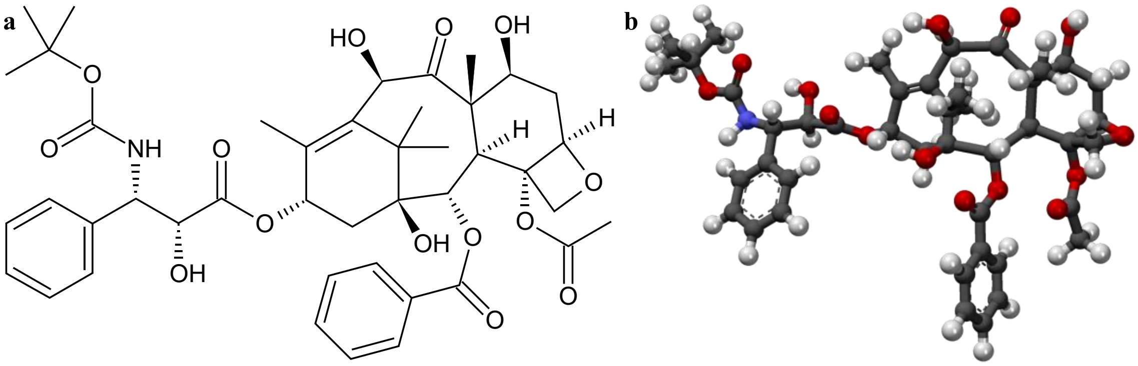

Figure 7: Structural diagram (**a**) and ball-and-stick model (**b**) of Docetaxel. Source: Wikimedia Commons

1.5 Docetaxel

Docetaxel (DTX) is a semi-synthetic drug derived from taxanes, originally identified in the Yew tree (genus *Taxus*). It is a commonly used chemotherapy drug for the treatment of a number of cancers including breast, stomach, prostate, and non-small-cell lung cancer.[38, 39] DTX was patented in 1986 and approved for medical use in 1995, and is considered to be one of the most effective and safe medicines needed in a health system. (WHO Model List of Essential Medicines). Trade names include TAXOTERE® and DOCEFREZ®. (BC Cancer Agency Cancer Drug Manual). Docetaxel's structure can be seen in **Figure 7**.

DTX acts as a radiosensitizer by blocking cells in G2 and Mitosis, the most radiosensitive phases of the cell cycle. DTX alone has shown remarkable radiosensitization both *in vitro* and *in vivo*.[40-43] It has also been investigated as a radiosensitizer in several Phase II clinical trials.[44-48]

1.5.1 Mechanism of Action

Docetaxel binds to β-tubulin and stabilizes it against depolymerization, while also lowering the critical concentration of tubulin necessary to form new MTs.[49] This causes unregulated formation of MTs, without regard to the MTOC.[50] DTX sequesters MTs in bundles hindering the formation of a mitotic spindle which is necessary for cell division (**Figure 8b**(**i**)).[51, 52] At mitosis, a normal cell forms a mitotic spindle out of microtubules, stretching between two 'asters' originating at centrosomes at either pole (**Figure 8a**(**ii**)). The DNA is arranged at a metaphase plate between the asters before the chromosomes are evenly separated into daughter cells (**Figure 8a**(**iii**)). With DTX treatment, asters and bundles are formed independently of centrosomes, creating multiple cleavage planes (**Figure 8b**(**ii**)). For example, 50nM DTX is sufficient to cause a 'mitotic catastrophe': the cell cannot enter anaphase and remains locked in mitosis or becomes multinucleate as the nuclear envelope reforms around the multiple asters (**Figure 8b**(**iii**)). This results in blocking the cell cycle at the G2/M phase.

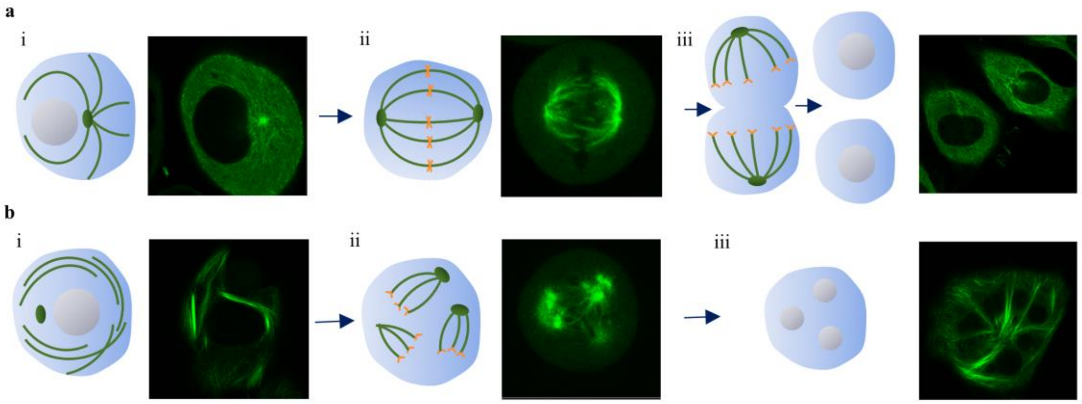

Figure 8: Schematic diagram and confocal images of microtubule structure showing cell division under control (**a**) and 50nM DTX (**b**) conditions.

a) i) Quiescent normal cell with microtubules (green) originating from the microtubule organizing centre (green ellipse), ii) normal mitotic spindle, iii) normal pair of daughter cells. **b)** i) Multiple aster formation in non-dividing cell with DTX, ii) fragmentary division with 10nM DTX, and iii) mitotic arrest with multinucleation under 50nM DTX. Schematics: Leah Cicon. Confocal Images: Own work.

1.6 State of the Field

Gold nanoparticle systems, while they have shown remarkable properties in vitro and in vivo, still require significant refinement before reaching widespread clinical use[24]. Currently, there are only two gold nanoparticle systems in clinical trials for cancer: one using Tumour Necrosis Factor-conjugated GNPs (NCT00356980 and NCT00436410 from www.clinicaltrials.gov), and one using gold nanorods for photothermal ablative therapy under the name Aurolase (NCT00848042 and NCT02680535). Neither is indicated for radiosensitization, nor have either yet made it to stage II trials. GNP-induced radiosensitization has been demonstrated in several cell lines and in murine models, however the sheer variety of sizes, shapes, and surface coating combinations being used make it difficult to determine what the optimal parameters would be for a clinical formulation.[24, 53] In addition, clinical use would require evaluation of dosing schedules, concentration, type of radiotherapy, and use with free or conjugated chemotherapy drugs[54].

While the only nanomedicines currently approved in the US are liposomal systems, there have been several preclinical studies of gold nanoparticle systems used for delivery of ligated chemotherapy drugs.[55] Few studies have looked at combined chemoradiotherapy using GNPs. Of these, most report lower toxicity in vivo than the free drug.[56-58] However, the combined therapeutic effect of GNP and drug is either reported as additive (cisplatin, bleomycin)[56, 59-61] or not evaluated for supra-additive effect or synergy (doxorubicin)[57, 58, 62, 63]. All three of these drugs affect the DNA directly and thus may compete with GNPs for efficacy.[60]

Due to its poor solubility in water, there has been significant research into nanoparticle formulations of Docetaxel to improve circulation time and lower the required dosage.[64-66] Only three studies found imaged intracellular nanoparticle distribution, though not along with the microtubule structure.[67-69] A few GNP-DTX formulations have been reported, though none have been evaluated for radiosensitization.[70-72]

1.7 Scope of Thesis

The goal of the study was to address two important challenges to the effective use of GNPs in future radiotherapy with DTX, a commonly used chemotherapy agent:

a) *How does the presence of DTX modulate uptake, distribution, and retention of GNPs in cancer cells?*

b) *How does the modulation of GNP uptake, distribution and in the presence of DTX affect outcome in radiotherapy? Does this agree with theoretical model predictions of GNP dose enhancement?*

Chapter 2: Methods

To address these challenges, MDA-MB-231 (ATCC# HTB-26) and HeLa (ATCC# CCL-2) cells were grown in culture and inoculated with docetaxel and GNPs synthesized and characterized in our lab. We quantified GNP uptake with ICP-MS and observed their intracellular distribution with live-cell fluorescence microscopy. The effectiveness of combined treatment with DTX, GNPs, and radiotherapy was evaluated by clonogenic assay and measurement of proliferation after treatment.

2.1 Gold Nanoparticles

2.1.1 Synthesis of Gold Nanoparticles

All listed reagents for GNPs were obtained from Sigma-Aldrich unless otherwise specified. Spherical gold nanoparticles were prepared via a modified citrate reduction method.[73] 11.5mL of 100nM NaOH (Fisher Scientific) was added dropwise to 1.29mL of 10% (w/v) chloroauric acid ($HAuCl_4 \cdot 3H_2O$). This was added to a beaker containing 117.5mL of double distilled water and brought to 90° C while stirring. 19.7mL of 1% sodium citrate tribasic dihydrate ($HOC(COONa)(CH_2COONa)_2 \cdot 2H_2O$) was added, and the temperature was reduced to 85° C. Temperature and stirring were maintained for 20 minutes as the solution first became a dark black/purple color, and gradually changed to a wine or cherry red color. The solution was then brought to room temperature while stirring.

2.1.2 Surface Functionalization of Nanoparticles

PEG-ylation was performed using polyethylene glycol-thiol (2kDa, Nanocs, Boston, USA) by adding to the nanoparticle solution in a ratio of 600 molecules/nanoparticle for 15nm nanoparticles. The ratio of molecules to surface area was preserved for larger nanoparticles, based on their diameter as measured by UV-Vis spectroscopy. A peptide with the integrin binding domain RGD (full sequence NH2-Cys-Lys-Lys-Lys-Lys-Lys-Lys-Gly-Gly-**Arg-Gly-Asp**-Met-Phe-Gly-COOH) (AnaSpec, San Jose, USA) was added to the solution at a ratio of 600 molecules/nanoparticle. The PEGylated and RGD-modified nanoparticle constructs will be referred to as GNPs.

For confocal imaging, PEG-ylation was performed with 300 molecules/nanoparticle of polyethylene glycol-thiol, and 300 molecules/nanoparticle of polyethylene glycol-thiol with a ligated Cy5 fluorophore (excitation 633nm, emission filter 650nm LP).

2.1.3 Characterization of Nanoparticle Complexes

2.1.3.1 Ultraviolet-Visible Spectroscopy

GNP complexes were characterized after production to determine properties such as size and charge. Size and concentration were measured using an Ultraviolet-Visible (UV-Vis) Spectrometry, which measures the absorbance of a sample to light in the ultraviolet (190-400nm) and visible (400-800nm) light regions of the electromagnetic spectrum. A schematic the Perkin-Elmer Lambda 365 spectrometer used can be seen in **Figure 9**. Light from a deuterium discharge lamp (ultraviolet) or tungsten-halogen lamp (visible) is passed through a slit, then onto a diffraction grating which splits the incident light, turning the beam into a fan of light with a gradient of wavelength across it. A particular wavelength from this fan is selected by another slit, and the resulting monochromatic beam is directed through a cuvette containing the sample of interest and into a photodetector. Cuvettes are sized to ensure a uniform 1cm light path length through the sample. A reference sample of

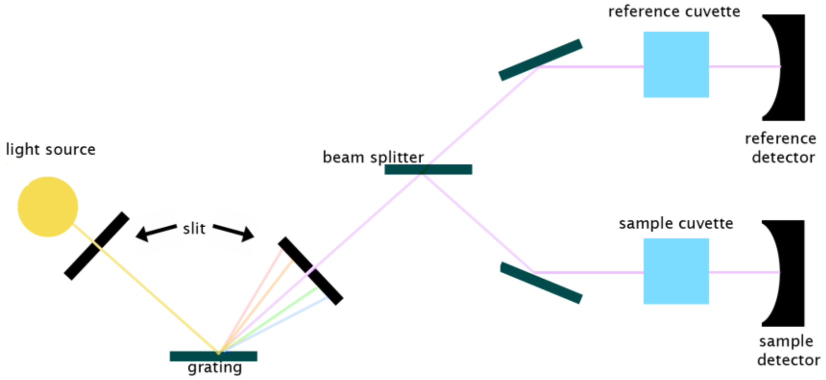

Figure 9: Schematic of ultraviolet-visible spectrometer. Image credit: Tristan Bannister

the solvent is used for comparison, either through simultaneous measurement by way of a beam splitter and second photodiode, or by sequential measurement on the same detector. In this case, a 2mL sample of bare or functionalized GNP solution was measured sequentially with a 2mL sample of deionized water as a reference. Polystyrene disposable or quartz low-volume cuvettes were used.

For each wavelength of a spectral scan, the intensity of transmitted light through the sample ($I(\lambda)$) and the reference ($I_0(\lambda)$) are measured. The absorbance ($A(\lambda)$) of the sample at a given wavelength is defined by the following equation:

$$A(\lambda) = \log_{10} \frac{\mathrm{I}_0(\lambda)}{I(\lambda)}$$

If I_0 is greater than I, then the sample has absorbed light and A is positive. In general, absorbance is proportional to the concentration of a substance in solution according to the Beer-Lambert law:

$$A = \varepsilon c l$$

Where A is absorbance, l is the optical path length (1 cm for cuvettes), c is the concentration of the solution (mol L^{-1}), and ε is the molar extinction coefficient (L mol^{-1} cm^{-1}) of the substance.

The absorption properties of spherical GNPs are related to their diameter by Mie theory, a solution of Maxwell's equations for calculating absorption and scattering coefficients of electromagnetic waves by spherical particles.[74] The diameter of GNPs in a reasonably monodisperse solution can be found with either its wavelength of peak absorption λ_{spr} (corresponding to a surface plasmon resonance) or the ratio of peak absobance to absorbance at $\lambda = 450\,\mathrm{nm}$ ($\frac{A_{\mathrm{spr}}}{A_{450}}$). Above a $25\,\mathrm{nm}$ diameter, the peak absorption wavelength can be fit to an exponential for both theory and experiment:

$$\lambda_{spr} = \lambda_0 + L_1 e^{(L_2 d)}$$

Where the fit parameters from theory derived by Haiss *et al* are $\lambda_0 = 512\,\mathrm{nm}$, $L_1 = 6.53\,\mathrm{nm}$, and $L_2 = 0.0216\,\mathrm{nm}^{-1}$ and d is the particle diameter in nm. The diameter from the absorbance ratio can also be found via an exponential fit:

$$d = \exp\left(B_1 \frac{A_{spr}}{A_{450}} - B_2\right)$$

Where $B_1 = 3.00$ and $B_2 = 2.20$. The absorbance at $\lambda = 450\,\mathrm{nm}$ is used because of good agreement between theoretical and experimental data, and this wavelength suffers less from effects of particle oblateness seen at $\lambda > 600\,\mathrm{nm}$. This wavelength also does not fall within the absorbance peak of any of the GNP sizes considered, so is somewhat independent of the surface plasmon effect.

Once the nanoparticle diameter is known, the absorbance A_{450} was used to determine nanoparticle concentration by the Beer-Lambert law, where molar extinction coefficients

$\epsilon_{450}(d)$ were obtained from a table provided by Haiss *et al* from the above Mie scattering model. For 15 nm GNPs, $\epsilon_{450} = 2.18 \times 10^8$ M^{-1}cm^{-1} and in a standard 1 cm path-length cuvette the concentration was determined as

$$C = \frac{A_{450}}{\epsilon_{450}}$$

These relations and fitting parameters are only valid for bare or citrate-capped GNPs in water, as adding surface layers or changing the medium may change the surface plasmon resonance and refractive index at the nanoparticle surface. [74]

2.1.3.2 Dynamic Light Scattering (DLS)

Measurements of GNP diameter from UV-VIS spectroscopy were confirmed via Dynamic Light Scattering (DLS). DLS measures the hydrodynamic diameter of particles, or the diameter of a hypothetical hard, non-charged sphere that diffuses at the same rate as the examined particle.

Large molecules or particles suspended in a fluid undergo Brownian motion, a random walk caused by collision with the rapidly moving molecules of the fluid. Because each collision is stochastic and independent of each other, the motion of different large particles in the fluid is uncorrelated. The variation in speed depends on the size of the particle, with larger particles accelerating more slowly than smaller ones. The hydrodynamic diameter may be larger than the actual diameter for particles with charge or complex surfaces. These pull solvent molecules along with them, increasing their effective size and drag through the fluid.

In DLS, laser light is shone into a cuvette containing a particle suspension, and a time series of the scattered light is collected by a fast photon counter. Brownian motion of the particles moving throughout the beam will change the amount of light reaching the detector. The fluctuations are characterized by means of a second-order autocorrelation function $g^{(2)}(\tau)$, which convolves the intensity signal with a time-delayed copy of itself. In the simplest case of a monodisperse suspension the translational diffusion coefficient D_t can be found by fitting an exponential decay:

$$g^{(2)}(\tau) = 1 + A\exp(-2D_t\tau/q^2)$$

Where τ is the delay time at which the autocorrelation is calculated, A is a correction factor depending on beam alignment, and q is the wave vector:

$$q = \frac{4\pi n_0}{\lambda}\sin\left(\frac{\theta}{2}\right)$$

Where λ is the laser wavelength, $n_0$is the refractive index of the solvent, and θ is the angle from the incident beam at which the scattered light is measured. More complex fits of the autocorrelation function are required for polydisperse samples, with the exact details varying by instrument and manufacturer.

The hydrodynamic diameter D_h can then be determined via the Stokes-Einstein equation for diffusion:

$$D_h = \frac{k_B T}{3\pi\eta D_t}$$

Where

- k_B is Boltzmann's constant,
- T is the absolute temperature of the sample,
- η is the dynamic viscosity of the solvent.

Measurements of hydrodynamic diameter were carried out using an Anton Paar Litesizer™ 500 instrument in polystyrene or low-volume quartz cuvettes. Model fits were performed using their cumulant algorithm and reported as an intensity-weighted distribution. Nanoparticles were suspended in deionized water at 25° C unless otherwise specified. Polystyrene cuvettes were disposed after use, and quartz cuvettes were rinsed with 70% ethanol and dried with 100% ethanol between uses.

2.1.3.3 Zeta potential (ζ)

The zeta potential of a particle is defined as the electrokinetic potential at the hydrodynamic radius or slip plane, where solvent molecules and ions are free to move around the nanoparticle rather than traveling with it. This is lower in magnitude than the actual surface charge of the particle due to screening effects of ions adsorbed or attracted to the surface.

Zeta potential was measured using electrophoretic light scattering, which measures the Doppler shift in scattered light due to the movement of particles in an electric field. The magnitude and phase of the Doppler shift can be related to the charge. The zeta potential can vary based on particle surface modification or ion concentration in the solvent, as this can affect the thickness of the immobile layer around the nanoparticle.

Zeta potential measurements were performed using an Anton Paar Litesizer™ 500 instrument in Omega capillary cuvettes. These cuvettes have a long capillary for the sample with electrodes at either end which produce the required electric field. The solvent for all zeta measurements was deionized water unless otherwise specified. Cuvettes were rinsed 3 times with deionized water and dried with compressed air between each use.

2.1.3.4 SEM imaging

Images of functionalized nanoparticles deposited onto carbon grids were taken using a Hitachi SU9000 Ultra-high Resolution Scanning Electron Microscope (SEM) (UVic Advanced Microscopy Lab).

2.2 Cell Culture

2.2.1 General Practices

MDA-MB-231 and HeLa cells were maintained in high-glucose DMEM (HyClone) supplemented with 10% FBS (Gibco) and 1% penicillin/streptomycin (Gibco). Media was aspirated and replaced with fresh stock every 3-4 days. Before reaching confluence, cells were washed with phosphate buffered saline (PBS, HyClone), trypsinized and replated at a passage ratio of 1:4 or 1:5. Cell cultures were discarded after 20 passages.

New cultures were prepared from 1 mL frozen stock by warming in a 38° C water bath, then suspending in 9 mL fresh media. The cell suspension was centrifuged at 350 g for 5 minutes, then the supernatant was poured off and the cells were resuspended in 10 mL

2.2.2 Docetaxel and GNP inoculation

6-well dishes were plated with 300k cells/well (MDA-MB-231) or 400k cells/well (HeLa). Due to significant cell death in HeLa cultures with DTX, samples with the drug were plated in 10cm dishes, 2m cells/dish. The next day, wells were inoculated with DTX (diluted from DMSO in PBS and media, DMSO concentration 0.04%v/v) to a final concentration of 50nM. Control wells were inoculated with DMSO carrier diluted via same method. All wells were inoculated with 15nm GNPs diluted in media to a final concentration of 0.2nM. Unless otherwise specified, inoculation with DTX and GNP-RGDs occurred concurrently, and exposure was carried out for 24h at 37°C.

2.3 Cytotoxicity Assay

The cells were seeded in black-walled clear-bottom 96-well plates (Costar) (10000 cells/well, 100µL media). Docetaxel was diluted from a stock solution of 0.10 mg/mL in DMSO (120µM) serially in DMSO. Each solution was further diluted 7.2:100 into PBS and then into media to the desired concentration. 24h after plating the media was aspirated and wells were rinsed with PBS. 100µL of DTX-containing media was added. The plates were incubated for a further 24 hours, then aspirated and rinsed again with PBS. 100µL of media containing 10%v/v resazurin dye (PrestoBlue, Thermo-Fisher) was added. Each plate was incubated for 3h at 37°C, then read in a Cytation plate reader. Fluorescence was measured using filters at Ex 530/25, Em 590/35 nm. Viable cells reduce the resazurin compound, and the fluorescence of the product correlates linearly to the number of viable cells.

The cytotoxicity response curve was fit using the Growth Rate Inhibition metric, which modifies the standard inhibitory concentration (IC) metric to account for the effects of slow division times comparable to the length of the assay.[75]

2.4 Cell Cycle Analysis

Cells were cultured and inoculated with DTX or GNPs as described in the Uptake section. After specified incubation period, cells were harvested using trypsin, fixed with 4% paraformaldehyde (Sigma-Aldrich) in PBS, permeabilized in ethanol, and stained with propidium iodide as described in by Yang et al.[61] Propidium iodide is a DNA-binding fluorescent stain, and the level of fluorescence is proportional to a cell’s DNA content. In a normal population most cells will be in G0 or G1 with one copy of their DNA (1N DNA content). G2 or M-phase cells will have 2N DNA content, while S-phase cells will lie in between as they are in the process of DNA replication. A histogram of fluorescence will show two peaks joined by a low middle region, as seen in **Figure 13c**, first panel (page 43). Stained cells were measured on a BD FACScalibur flow cytometer, and a Dean-Jett-Fox cell cycle model fit was applied in the accompanying FlowJo software.

2.5 Nanoparticle Uptake Study

2.5.1 Procedure

To measure release and redistribution of nanoparticles, samples were prepared as in section 2.2.2. Following inoculation and exposure, the media was removed, and cells were gently washed 3 times in PBS to remove any gold not trapped within cells. Fresh media was added, and cells were incubated for a further 24 hours.

After 24h incubation (uptake) or 24h incubation and 24h fresh media (retention), the media was aspirated. Each dish was gently washed 3 times with PBS, then cells were detached with 1mL of 0.25% Trypsin-EDTA (Gibco). Cell concentrations were counted using an automatic cell counter (Z2 Coulter from Beckman Coulter) with a 100uL sample of the suspension and confirmed manually using a trypan blue exclusion assay in a hemacytometer. The remaining solutions were processed with aqua regia (3:1 mixture of HCl and HNO_3 (VWR)) in a heated mineral oil bath until solutions were clear with no visible debris or turbidity and diluted to 4% v/v acid content with deionized water. Gold concentration was measured using Inductively Coupled Plasma – Mass Spectrometry (ICP-

MS) (Optima 7300 DV, Perkin Elmer, Waltham, USA). Standard solutions of gold chloride were prepared along with samples and used to generate a calibration curve.

The following equations were used to process the data from ICP-MS measurement, related in parts per billion (ppb) or ng/mL:

$$\frac{\#GNPs}{cell} = \frac{Au\ concentration\ [\mathrm{g\,mL^{-1}}] \times Sample\ volume\ [\mathrm{mL}] \times N_A\ [(\mathrm{mol\,GNP})^{-1}]}{Au\ molar\ weight\ [\mathrm{g\,(mol\,Au)^{-1}}] \times Total\ \#\ cells\ [\mathrm{cell}] \times GNP\ ratio\ [(\mathrm{mol\,Au})\,(\mathrm{mol\,GNP})^{-1}]}$$

Where N_A is Avogadro's number and the GNP ratio is given by

$$GNP\ ratio\ \left[\frac{\mathrm{mol\,Au}}{\mathrm{mol\,GNP}}\right] = \frac{Atoms\ per\ unit\ cell^{*} \times GNP\ volume\ [\mathrm{nm^3}]}{Unit\ cell\ volume\ [\mathrm{nm^3}]}$$

$$= \frac{4 \times \frac{4\pi}{3}\left(\frac{D}{2}\right)^3}{a^3} = \frac{2\pi}{3}\left(\frac{D}{a}\right)^3$$

Where D is the core diameter of a spherical nanoparticle and a is the length of a crystal lattice cell, $0.408\ \mathrm{nm}$*. These calculations assume an even distribution of nanoparticles per cell, and thus only represent an ensemble average.

*Gold nanoparticles synthesized through citrate reduction form face-centred cubic (fcc) lattices, where each unit cell (the smallest repeating unit) contains four atoms.[76]

2.6 Confocal Imaging

Live-cell imaging of nanoparticle uptake and DTX action was performed using a laser scanning confocal microscope (NIKON Eclipse TE2000-U). GNPs were functionalized with PEG, RGD, and a PEG-Cy5 complex (excitation 633nm, emission filter 650nm LP). α-tubulin was labeled with a viral transfection stain (CellLight Tubulin-GFP, BacMam 2.0, obtained from Thermo-Fisher). The virus contains DNA coding for an α-tubulin/GFP fusion construct. This creates both free and polymerized fluorescent tubulin, leading the control cells to appear uniformly red outside of the nucleus. This method was chosen as all other live-cell tubulin stains investigated are taxane-based and would compete with docetaxel for binding sites.

Cells were cultured in 3cm coverslip-bottomed dishes (MatTek, Ashland, MA) in FluoroBrite DMEM (Gibco) supplemented with 10% FBS (Gibco) and 1% penicillin/streptomycin (Gibco). Cells were incubated for >24h with the viral stain before DTX and fluorescent GNPs were added to the media. Dishes were removed in groups of 2 from the incubator for imaging sessions of less than 2h. Cells were imaged at time points of 4h, 24h, and 48h after inoculation before exchanging the media to remove DTX and GNPs, then again 24h later to observe exocytosis.

Images were taken at 60x and 100x magnification, with settings held constant for images at the same magnification. Image processing was performed using ImageJ. As the viral stain transfection efficiency was low, and individual cell brightness varied, the tubulin channel (red in images) brightness was selected to allow for the maximum number of visible and unsaturated cells. GNP channel brightness was scaled to show distribution (not quantity) of GNPs unless otherwise mentioned.

Figure 10: Image of treatment geometry

2.7 Radiation

2.7.1 Procedure

Cells were prepared in 6-well plates and inoculated as described above. After 24h of incubation, the plates were placed between two 5cm solid water block at the isocenter of a Varian TruBeam medical linear accelerator and irradiated with a 6MV beam (28cmx28cm field size, 202 monitor units) (**Figure 10**). A 6MV beam was chosen due to its common clinical use. The 5cm solid water blocks were used to mimic the conditions in a deep-seated tumour, including the beam contamination with lower-energy x-rays as a consequence of passing through other tissue. Most clinical RT treatments are given in fractions of 2Gy, thus this the prescribed dose used here. The planned monitor unit setting for this irradiation was calculated as follows, for a reference point at the base of the culture plate ($d = 5$ cm):

$$Prescribed\,MU = prescribed\,dose\,[\text{Gy}] \times dose\,coefficient\,[\text{MU Gy}^{-1}]$$

$$= \frac{prescribed\,dose\,[\text{Gy}]}{RDR \times TMR \times S_c \times S_p}$$

Where:

RDR = reference dose rate = 1 cGy MU^{-1}

TMR = tissue maximum ratio = $TMR(\text{6MV}, 28 \times 28, d = 5) = 0.925$

S_c = collimator scattering factor = $S_c(\text{6MV}, 28 \times 28) = 1.041$

S_p = phantom scatter factor = $S_p(\text{6MV}, 28 \times 28) = 1.031$

For 2 Gy or 200 cGy and a calculated dose coefficient of 100.95 MU Gy^{-1}, we delivered 202 MU.

Control cells were transported to the linear accelerator, but not irradiated. The cells were returned to the incubator to rest for 1 hour after irradiation, then trypsinized and counted using both an automatic cell counter and manually via trypan blue exclusion assay (Gibco) on a hemacytometer. The resulting cell suspensions were used for the clonogenic and proliferation assays described below.

2.7.2 Clonogenic Assay

The cell suspensions were replated into 10cm dishes at seeding densities of 500/dish for CTL and GNP, 40000/dish for 50nM DTX and 50nM DTX+GNP due to much lower survival fraction. These plates were incubated for 14 days, then resulting colonies were stained with methylene blue (BioShop) and manually counted via microscope. The number of colonies of 25 or more cells vs. plated cells was normalized by the plating efficiency of control cells to obtain the survival fraction. Two-way analysis of variance of irradiated samples was performed using the CFAssay package for R.[77, 78]

2.7.3 Proliferation Assay

Cells from the radiation experiment were seeded into three black-walled clear-bottom 96-well plates (Costar) (10^3 cells/well, 100 µL fresh media) and covered with a breathable membrane to reduce evaporation (Breathe-Easier Membranes). At the time of the reading, the membrane was removed and the media was aspirated. 100 µL of media containing 10% v/v resazurin dye (PrestoBlue, Thermo-Fisher) was added to each of the well followed by incubation for 1 hr. Fluorescence was measured using Biotek Cytation 1 plate reader (filters at Ex 530/25, Em 590/35 nm). Viable cells reduce the resazurin compound, and the fluorescence of the product correlates linearly to the number of viable cells.

2.8 Monte Carlo Simulation

Monte Carlo simulations were performed by Wonmo Sung and Jan Scheumann of Massachusetts General Hospital and Harvard Medical School. Monte Carlo simulations were performed using the TOPAS/TOPAS-nBio version 3.1.p2.[79, 80] Therapeutic x-rays from a 6 MV Varian TrueBeam linear accelerator attenuated through 10 cm of water were incident to a single 15 nm GNP and the radial dose was calculated. As in our previous studies [32, 81, 82] , the radial dose was superimposed on each GNP location in the cell. The cells were represented by elliptical shapes with major/minor diameters of 18.5/8.5 μm. The size of the cell nucleus was assumed to be 8 μm. The GNPs were encapsulated inside vesicles of 50 nm diameter, with 10 GNP per vesicle. The vesicles are distributed in the cytoplasm either uniformly or exponentially for cells without or with docetaxel, respectively. The radial dose enhancement was scored inside the nucleus.

An adapted local effect model was introduced to predict survival fractions. Radiation response parameters of α = 0.019, β= 0.052 and α = 0.282, β= 0.087 were assumed for MDA-MB-231 and HeLa cells, respectively [40, 83] .

Chapter 3: Results & Discussion

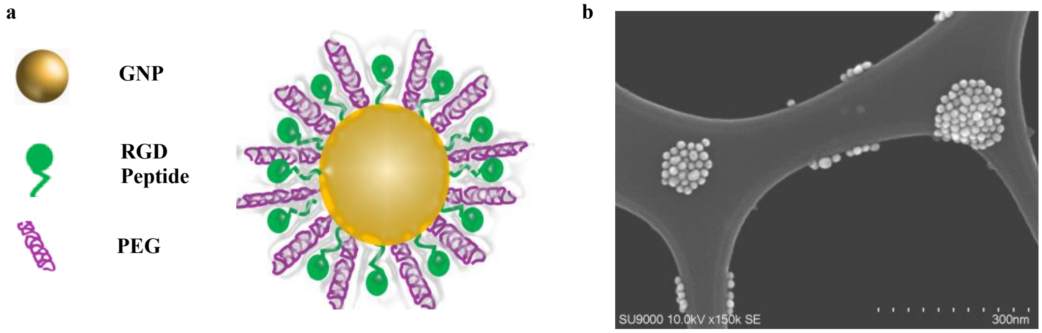

Figure 11: GNP functionalization.
a) Schematic diagram showing the presence of both RGD-peptide and PEG on GNP surface. **b**) SEM image of functionalized GNPs.

3.1 Gold Nanoparticle Characterization

Gold nanoparticles used for this study were functionalized with polyethylene glycol (PEG) and a peptide containing the integrin binding domain RGD (RGD peptide) as illustrated in **Figure 11a**. Having PEG is necessary to improve the circulation life time for their optimum entrapment within the tumor using its leaky vasculature.[84] However, having PEG on the GNP surface would reduce their uptake once they reach the tumor cells. Hence, we added a peptide containing integrin binding domain, RGD to increase the uptake of GNPs. To enhance receptor-ligand interaction, we used smaller 15 nm diameter GNPs as the high curvature of smaller GNPs improves the interaction between RGD-peptide and integrin on the cell membrane.[85] The size and shape of GNPs used in this study were measured with scanning electron microscopy (SEM) as shown in **Figure 11b**. These nominally 15 nm GNPs were 17.2 ± 5.6 nm in diameter.

A fresh batch of nanoparticles was made and functionalized for each experiment, and the average diameters varied between 11 and 18 nm. GNPs have a red color in solution, due to a surface plasmon resonance scattering: peak whose wavelength is determined by their diameter. The shape of the ultraviolet-visible (UV-VIS) spectrum for bare *vs.* PEG+RGD modified GNPs did not change appreciably, though the peak wavelength did shift slightly to the red (**Figure 12a**) since both RGD-peptide and PEG molecules were considerably smaller than the nanoparticle. For example, molecular weight of RGD-peptide and PEG were 1760 and 2000 Da, respectively. However, the addition of PEG and RGD peptide resulted in a slight change in hydrodynamic diameter along with a significant change in the surface charge as shown in **Figure 12b** and **c**. This is due to replacement of negatively

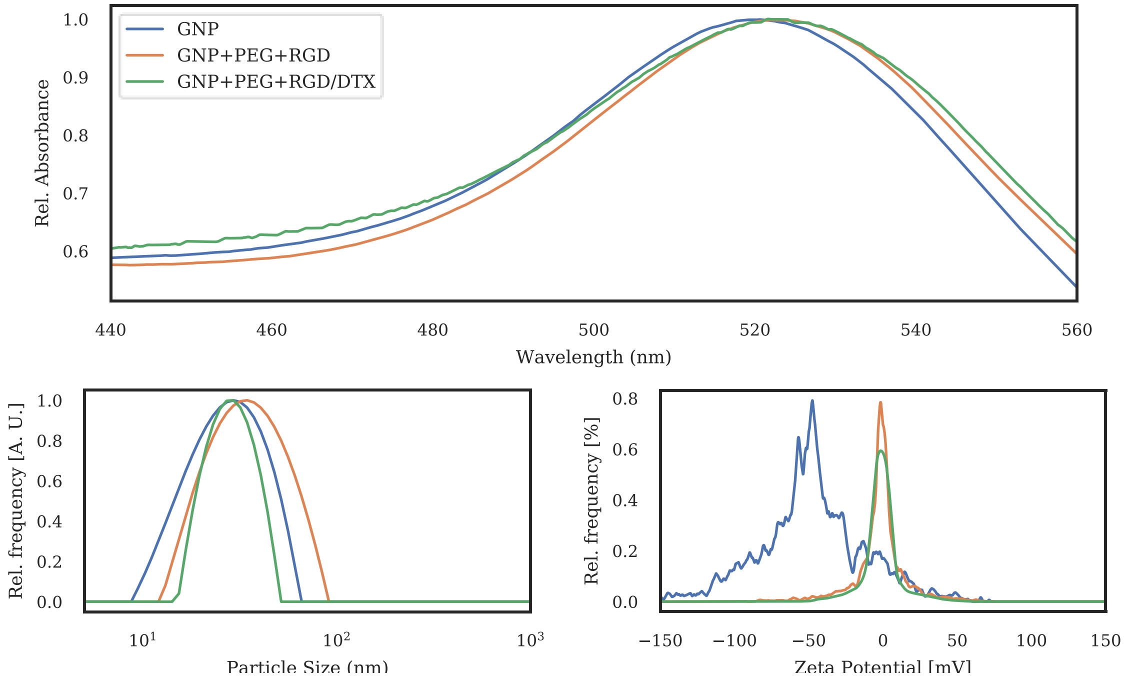

Figure 12: Characterization of bare nanoparticles (GNP), functionalized nanoparticles (GNP+PEG+RGD), and functionalized nanoparticles in DTX solution (GNP+PEG+RGD/DTX). Legend is identical for all plots. **a**) UV-VIS absorbance spectrum normalized to wavelength of peak absorption. **b**) Hydrodynamic diameter measurement from DLS. **c**) Zeta potential distribution.

charged citrate molecules with neutral PEG and positively charged RGD peptide molecules.

GNPs were also measured in a 50 nM DTX solution. The peak and shape of the UV/VIS spectrum or the surface charge of GNPs when in solution with DTX was not significantly changed, and the measured hydrodynamic diameter shrank slightly. The DTX was diluted into PBS and contained some of the DMSO from the working solution. A cuvette of this solution was used as a reference for the corresponding UV-VIS spectrum, and the refractive index of PBS was used for the DLS and Zeta potential modeling. The narrowing of the size distribution in DLS (**Figure 12b**, green line) may be due either to the higher ionic concentration of the solvent, or due to a change in refractive index and viscosity due to the DMSO. The fitting function for the autocorrelation in DLS depends on the inverse square of the refractive index, so a small change may significantly affect the results. Regardless, there remained only a single peak near the size of the bare nanoparticles with no evidence of a second peak at a larger diameter that would indicate aggregation. This is supported by the minimal shift in the spectral peak. While DTX adsorption cannot be ruled out, we have shown that DTX does not sufficiently modify the GNPs' surface properties to cause aggregation.

Functionalization	Peak Absorption Wavelength (nm)	Hydrodynamic Diameter (nm)	Zeta Potential (mV)
GNP	518.95 ± 0.05	23.59 ± 9.45	-51.2 ± 4.0
GNP+PEG	521.05 ± 0.05	32.11 ± 9.40	-13.6 ± 1.2
GNP+PEG+RGD	522.20 ± 0.05	37.31 ± 12.06	-3.1 ± 0.3
GNP+PEG+RGD/DTX	523.85 ± 0.05	29.01 ± 7.62	-0.4 ± 1.3

Table 1: Summary table of GNP properties with changes in functionalization.

3.2 Cytotoxicity Assay

To identify the optimal dosage of free DTX to use in the GNP uptake study, a cytotoxicity assay was performed. HeLa (cervical cancer) and MDA-MB-231 (breast cancer) cells were chosen for this study. Both HeLa and MDA-MB-231 are widely used for drug research, previous work with our nanoparticle system has been performed with both cell lines. [82, 86]

Dosages as high as 60 µM have been investigated through some *in vitro* work, though with diminishing returns beyond 600 nM.[87, 88] Hence, the dose range chosen for our

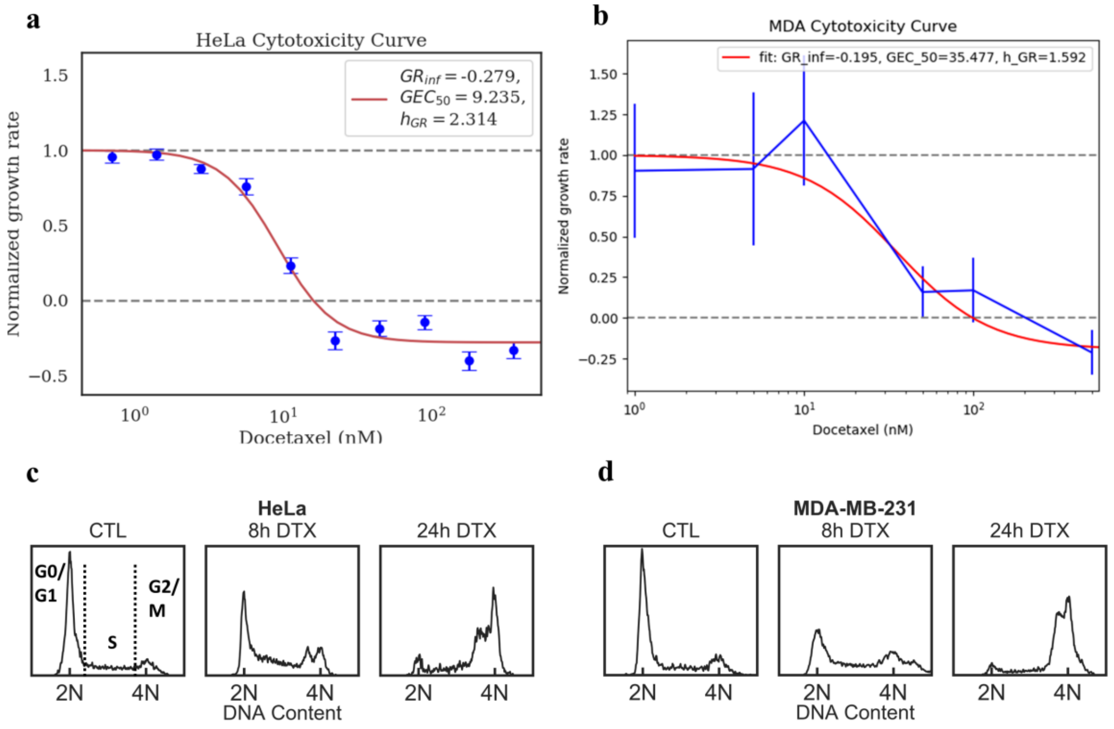

Figure 13: Cytotoxicity and cell cycle modulation due to Docetaxel (DTX).
a, **b)** Docetaxel cytotoxicity curves for HeLa (**a**) and MDA-MB-231 (**b**). Normalized growth rate is calculated to account for the different division times of the two cell lines. Growth rate = 0 represents complete cytostatic effect, growth rate < 0 represents cytotoxicity. Error bars are the standard deviations from at least three replicate experiments. **c,d)** Cell cycle distribution for HeLa (**c**) and MDA-MB-231 (**d**) with 8 and 24h DTX exposure at 50nM. Phases labeled by DNA content in control population. Ticks on bottom axis represent 2N (G0/G1) and 4N (G2/M) DNA content. Y-axis is normalized to total counts for each measurement.

assay was 0.5-500 nM (0.40-400 ng/mL) at 24 hours of exposure to identify the heel of the dose response curve (**Figure 13a, b**).[87] DTX shows cytotoxic effect (rather than just antiproliferative) at 10 nM, with the curve leveling off past 50 nM for both MDA-MB-231 and HeLa. Hence, the dose chosen for this study was and 50 nM. We believe such concentrations are clinically feasible within the tumor, based on pharmacokinetics of DTX.[89] Over a 24h exposure, the area under the concentration-time curve ($AUC_{0\rightarrow 24}$) of 1200 nM·h in media is similar to the $AUC_{0\rightarrow 24}$ for low-dose (20-30 mg/m^2) weekly clinical treatments of the type being investigated for use with radiation.[89, 90]

3.3 Cell Cycle Analysis

Before moving to uptake studies, we analyzed the variation of cell cycle and growth in the presence of DTX. The DNA content of cells exposed to 50nM DTX was measured using flow cytometry. Cells were arrested in mitosis and did not divide, collecting in the

Cell Line	Exposure	Time (h)	%G0-G1	%S	%G2-M	#cells	RMSD
HeLa	CTL	-	47.3	40.9	10.5	8227	3.2
	GNP	24	53.1	31.4	14.3	9722	2.98
	50nM DTX	8	21.7	47.5	31.1	9625	3.72
	50nM DTX	24	13.5	1.15	89.1	1997	1.7
	50nM DTX†	24+24*	64.4	-4.4	47.4	10928	3.06
MDA-MB-231	CTL	-	49.5	36.1	13.9	9666	3.71
	GNP	24	48.2	31.5	19.1	9939	3.04
	50nM DTX	8	26.2	42	32.6	9768	3.15
	50nM DTX	24	7.47	1.84	89.8	9557	4.26
	50nM DTX†	24+24*	25.5	16.6	55.8	10120	4.6

Table 2: Cell cycle data for exposure to 50nM DTX or 0.2nM GNPs, as fit by a Dean-Jett-Fox algorithm. GNP exposure for 24h did not appear to significantly alter the cell cycle distribution. Exposure to DTX caused a ~90% accumulation in the G2-M phase over 24h, with ~50% of cells remaining blocked after removal of the drug. * indicates exposure for 24h in DTX-containing media, then 24h in fresh media with no drug. † indicates a poor fit, the G1 peak was absent or obscured by significant sub-G0 debris. See **Figure 13d,e**. The root-mean-square deviation (RMSD) is a relative goodness-of-fit measure.

G2/M phase as evidenced by the peak at 2N DNA content. (**Figure 13c** and **d**, Error! Reference source not found.). This is consistent with previous studies for this dose range and exposure time.[40, 89, 91-93]

3.4 Effect of Docetaxel on Nanoparticle Uptake

Cellular uptake of modified GNP complexes was characterized using HeLa and MDA-MB-231 cells. HeLa (doubling time $T_d = 31h$) is a human cervical cancer line and MDA-MB-231 ($T_d = 40h$) is a triple-negative human breast cancer cell line. The concentration of DTX used for *in vitro* experiments was 50 nM. One of the highlights of our approach is that we use a clinically feasible 0.2 nM concentration of GNPs for this study. For example, our approach would require an intravenous administration of a few mg/kg of gold instead of g/kg, making it a potentially clinically relevant approach in the near future.[24, 94]

These NPs are internalized by receptor-mediated endocytosis and trapped in endosomes. These are transported to the perinuclear region, where they fuse with lysosomes for processing. The waste products are collected into vesicles which are then brought to the cell periphery for excretion (left side of **Figure 14a**).[95, 96] Studies have shown that microtubules are not involved directly in endocytosis; however the vesicle transport of NPs depends on the microtubule network.[52] Recycling of integrin binding receptors to the cell surface can occur before the endosome begins to move along a microtubule.[97, 98] Hence when the microtubule network is disturbed in the presence of DTX, the endocytosis process should be largely undisturbed while the transport of GNPs within the cell may be affected (right side of **Figure 14a**).

Nanoparticle uptake with exposure to 50 nM Docetaxel was measured using Inductively Coupled Plasma Mass Spectroscopy (ICP-MS) (**Figure 14b**). The nanoparticle load seen for untreated HeLa cells ($3.06 \times 10^5 \pm 0.15 \times 10^5\ \mathrm{GNP/cell}$) is similar to that seen in previous work by this lab for the same GNP concentration, size, and functionalization.[59, 61, 82] Both HeLa and MDA-MB-231 treated with DTX had a ~70% increase in uptake after 24 hours of incubation (**Figure 14b**). Over a period of roughly half a cell cycle, both cell lines show at least a 2-fold increase in the G2/M-phase population with the treatment of DTX (**Figure 17a,b**). The cells in G2/M phase are expected to have higher number of GNPs compared to other phases since the cell has more time to accumulate GNPs before division. Cell division dilutes the per-cell GNP load between daughter cells.[99] Hence, having more cells in G2/M could led to higher average number of GNPs within the whole cell population. Thus, we believe that the observed increase in uptake is likely due to DTX halting cell division at G2/M phase and preventing redistribution.

Confocal images were taken of cells after 24h of exposure to GNPs and DTX or vehicle control. We observed that there was a change in the cell morphology from elliptical (**Figure 14c, e**) to circular **(Figure 14d, f**) with the treatment of DTX for both MDA-MB-231 and HeLa cell lines. We believe that this change in the shape of the cells is due to the stabilization of microtubules with the addition of DTX, as described in the introduction. A significant difference in distribution of GNPs was seen in cells treated with DTX, where GNPs seem to distribute closer to the nucleus as shown in **Figure 14d, f**. This pattern of distribution of GNP clusters is consistent across several planes of the cell, as shown in **Figure 15** and **Appendix 1.1**.

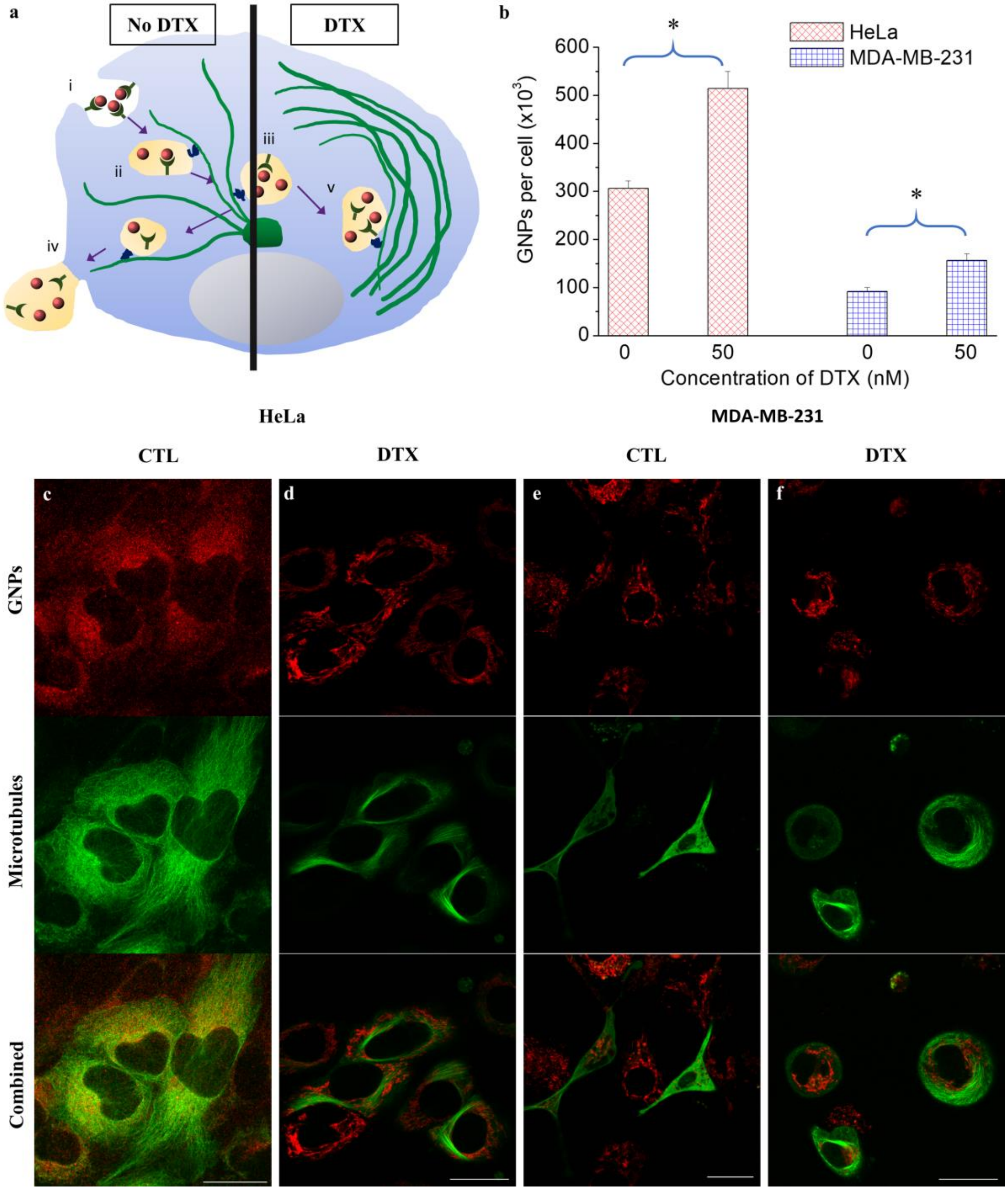

Figure 14: Cellular uptake of GNPs in MDA-MB-231 and HeLa cells.

a) Schematic diagram illustrating the path of GNPs (red dots) within a cell in the absence and presence of DTX, showing i) endocytosis, ii) vesicle transport, iii) processing near microtubule organizing centre (MTOC, green patch), and iv) exocytosis. **b)** Quantification of GNP uptake in the presence of 50 nM DTX (24 hr exposure). Error bars are standard deviations from 3 replicate measurements. *Represents a statistically significant difference from control (Welch's unequal variance t-test, $p<0.05$). **c-f)** Optical images of distribution of GNPs and MTs in HeLa **(c-d)** and MDA-MB-231 **(e-f)** cells treated with vehicle control (**c, e**) and 50nM DTX for 24h (**d, f**). The scale bar is 25 µm. GNPs are shown in red and MTs are shown in green. The scale bar is 25 µm.

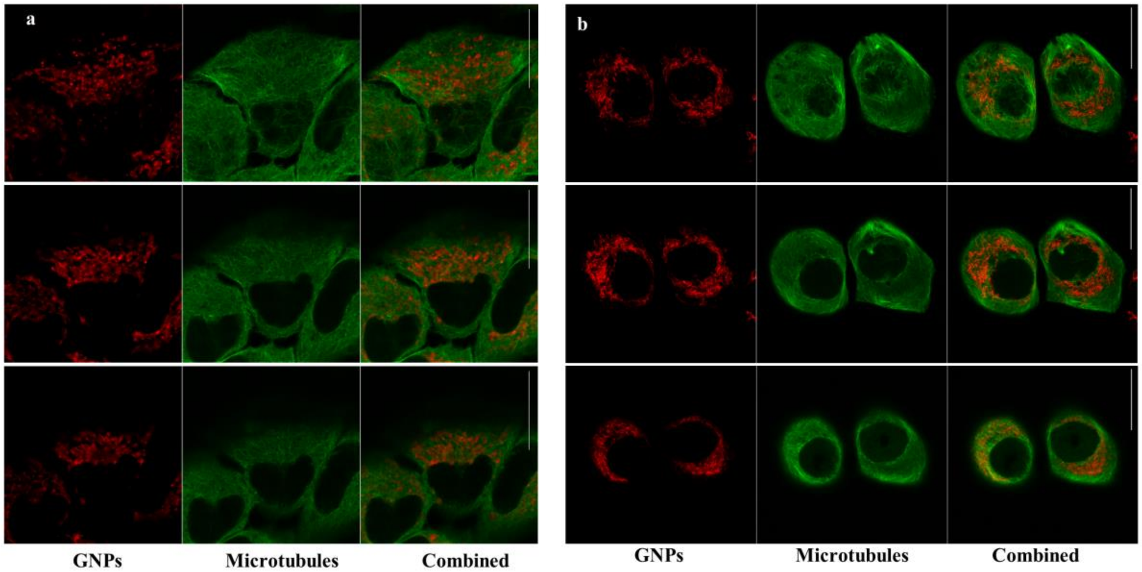

Figure 15: Confocal Z-stacks of HeLa cells.

a) Vehicle control treated. **b)** 50nM DTX-treated. GNPs are shown in red and MTs are shown in green. The scale bar is 25 μm. Slices are separated by 1.5 μm.

3.4.1 Dose and Time-dependence of Uptake

Considering over 60% increase of GNP uptake in the presence of DTX, the dose- and time-dependence of GNP uptake was investigated with MDA-MB-231 cell line. A comparison between cells exposed to 1nM *vs.* 50 nM DTX with GNPs (**Figure 16a**) shows no uptake enhancement at the lower dose. DTX is known to have a different effect on the cell cycle at low doses (~1nM), rather than halting cells in G2/M it causes uneven division and a significant population of sub-G0 cells (with less than a full DNA complement).[91, 100] This would cause the same dilution of GNPs through division expected in a control population, though whether intracellular distribution would resemble the high-dose DTX case is unknown. In cells inoculated first with 50 nM DTX and with 0.2nM GNPs 6h later, the enhanced uptake effect is halved compared to concurrent inoculation after 24 hours (**Figure 16b**). Endocytosis briefly ceases during the early phases of mitosis in normal cells,

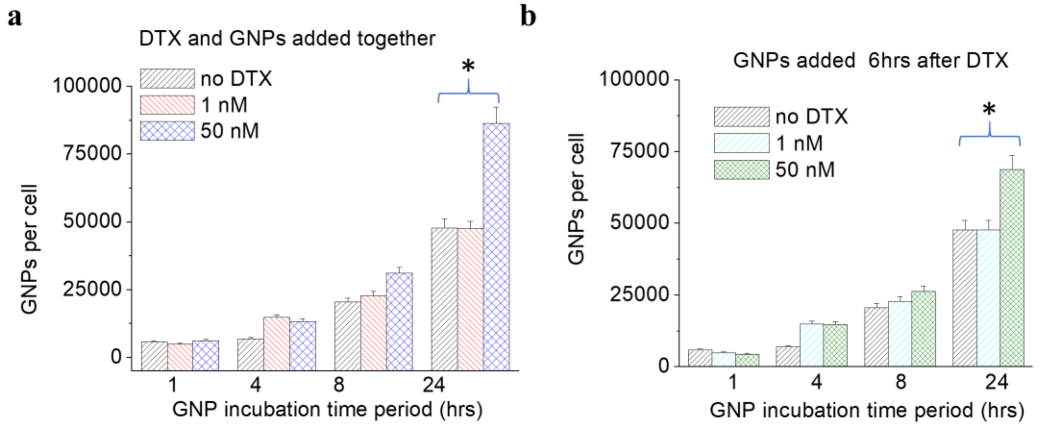

Figure 16: Dose- and Time-dependence of nanoparticle uptake.

a) Time dependence of uptake for concurrent administration of GNPs and DTX. **b)** Time dependence of uptake for GNPs administered 6h after DTX. Error bars represent standard error of 3 replicate samples. *Represents a statistically significant difference from control (Welch's unequal variance t-test, $p<0.05$).

and DTX may be halting cells during this phase. As the population of cells in G2/M doubles after only 8h of exposure (**Figure 13c, d**), this may cut off the potential for uptake of a significant fraction of cells before the GNPs are added. This implies that timing of treatment in a clinical setting will require further research to optimize uptake and retention. This experiment was performed only for MDA-MB-231 as the experiment and processing take 2 weeks for each cell line and dosage.

3.5 Retention of GNPs in the presence of DTX

Our results in **Figure 17a** demonstrate that the proportion of GNPs excreted or redistributed was reduced dramatically in cells treated with DTX. The percent of retention was between ~90-100% for both MDA-MB-231 and HeLa cells after 24 hours. Chithrani and Chan showed that exocytosis can occur rapidly after the nanoparticle-containing media is replaced, with up to 40% of internalized NPs being released within 4 hours for transferrin-coated GNPs.[95] If exocytosis moderates the uptake rate in normal cells, blocking that process may lead to an increased presence of NPs within cells. The observed

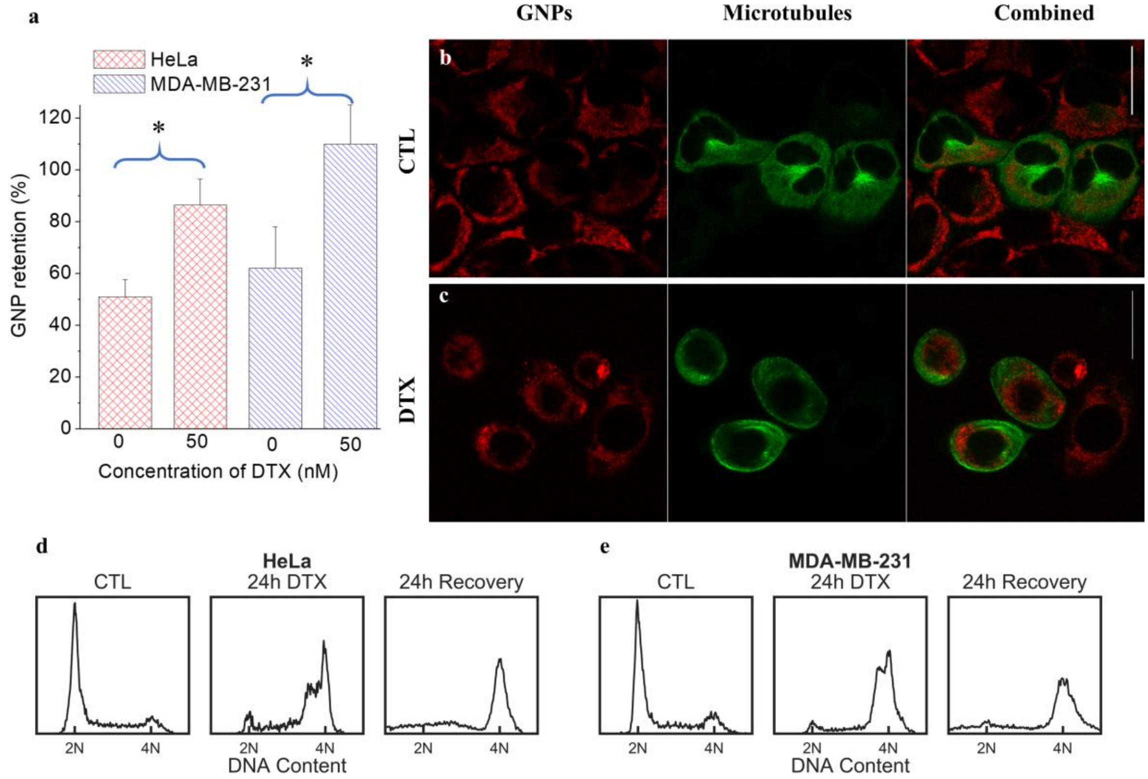

Figure 17: Retention of GNPs after exposure to DTX.

Quantitative (a) and qualitative (b-c) measurement of GNP retention 24h after release from DTX and GNP dosage. a) Percent retention of GNP load as compared to uptake for same DTX dosage. *Represents a statistically significant difference (Welch's unequal variance t-test, $p<0.05$). Error bars are standard deviations from 3 replicate measurements. b-c) Confocal images of HeLa cells after vehicle control (b) or 50nM DTX (c) exposure and release. GNPs represented in red, MTs in green. The scale bar is 25 µm. d-e) Cell cycle distribution after 24h with and further 24h release from 50nM DTX compared to vehicle control exposure for HeLa (d) and MDA-MB-231 (e) cells.

drop in cell GNP content for both MDA and HeLa control samples (without the treatment of DTX) is consistent with redistribution via division following an exponential with decay constant of ln2/ T_d. [99] The retention observed in the DTX treated cell samples is consistent with both a lack of redistribution and a cessation of exocytosis. **Figure 17b** and **c** show that the population of cells remains locked in G2/M even after 24 hours in drug-free media, supporting the lack of redistribution hypothesis.

In normal cells (**Figure 17d**), MTs are polarized to allow directed inward or outward motion.[101] When microtubules are stabilized, the processing of \vesicles containing

GNPs is disturbed.[50] It is necessary for NPs in the endosomes to be processed by fusing with lysosomes; however, the azimuthal microtubule bundles formed in the presence of DTX may not link endosomes with lysosomes efficiently. Even if the vesicles are processed, the lack of radially directed microtubules prevents them from moving to the cell surface for exocytosis. This would result in retarded outward motion of NPs and piling up NPs closer to the nucleus as shown in **Figure 17e**. For example, we noticed that some of these vesicles collect at the ends of bundles and in ‘empty’ regions, perhaps through diffusion after reaching the end of a microtubule (see **Appendix 1.2**). Or it could be that these MT bundles are similarly polarized as well as parallel. Vesicles may encounter only ends that direct them back into the empty regions not allowing them to reach the cell surface. The distribution of GNPs about the nucleus with DTX seen in **Figure 14d** was also observed in **Figure 17e**, with the endosomes apparently collecting in regions between the strained microtubule bundles and the nucleus.

There was a change in distribution of GNPs observed during mitosis, as shown in **Figure 18 a** and **b**. GNPs were excluded from the mitotic spindle apparatus in control cells, while in DTX treated cells their distribution was less regular. In the Monte Carlo simulations described below, only cells in interphase were considered as cells already in aberrant mitosis were considered to be nonproliferative. Further work, including localization of chromatin in these cells, is needed to model any additional effect the GNPs may have in this phase. If the GNP-containing vesicles are able to enter the chromatin-containing region, or if the chromatin is separated into multiple mitotic plates, then more DNA would be in close range of GNPs and additional radiosensitization would be expected.

No toxic interaction was observed between GNPs and DTX without radiation, as shown in **Figure 18c**. The addition of GNPs did not significantly alter the survival fraction from DTX.

3.6 Triple combination of GNPs, DTX, and RT

Linear accelerators are used to treat cancer patients in the clinic. Therefore, we used a model set up as illustrated in **Figure 19a**. Our samples were placed between solid water blocks to mimic a deep-seated tumor in a patient. A radiation dose of 2 Gy with a 6 MeV photon beam resulted in a further 30% decrease in survival vs radiated control when GNPs were incorporated within cells (**Figure 19c**). Our results are consistent with previously published data.[61, 83] Addition of GNPs into the RT/DTX combination resulted in an additional 50% decrease in long term cell survival vs RT/DTX (**Figure 19d**). This extra

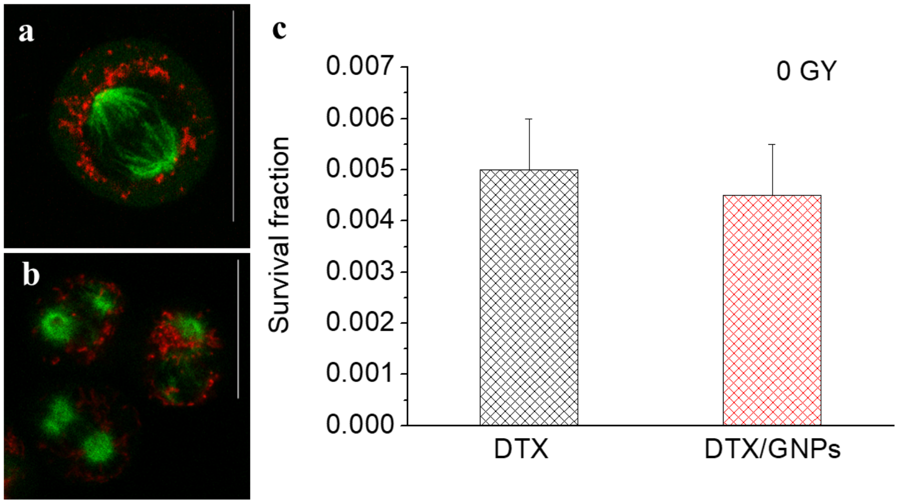

Figure 18: Non-radiation interaction of GNP and DTX and GNP localization during division. **a,b)** Confocal images of dividing HeLa cells under control (**a**) and 50nM DTX (**b**) treatment. GNPs are shown in red, microtubules in green. The scale bar is 25 μm. **c**) Survival fraction of non-radiated cells under DTX and DTX+GNP treatment from clonogenic assay. Error bars are 95% confidence intervals from Poisson model of 3 replicate measurements.

drop in survival indicates an interaction between DTX and GNPs that heightens radiosensitivity beyond an additive effect (p=0.0298). This improves upon other GNP-chemoradiation combination treatments with cisplatin and bleomycin, which saw only an additive effect for radiosensitivity. [59, 61] Hence, the triple combination of DTX, GNPs, and RT could play a major role in the reduction of normal tissue toxicity. Monitoring of the short-term proliferation of cells shows similar trend as illustrated in **Figure 19 e, f.**

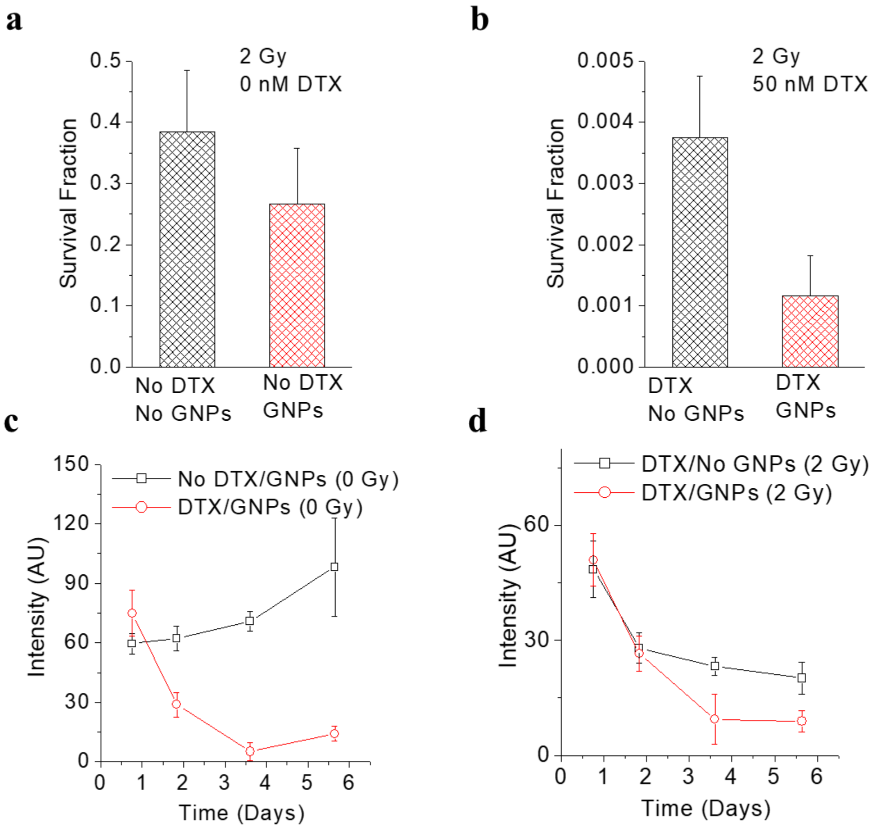

Figure 19: GNP, DTX, and RT combined treatment.

a) Relative survival fraction of vehicle control treated and irradiated HeLa cells with and without GNPs as determined by clonogenic assay. **b)** Relative survival fraction of 50nM DTX-treated and irradiated HeLa cells with and without GNPs as determined by clonogenic assay. **c)** Proliferation curves of non-irradiated HeLa cells after treatment with GNPs, with or without DTX. **d)** Proliferation curves of irradiated HeLa cells after treatment with DTX, with or without GNPs. * indicates interaction between treatment conditions from Two-Way ANOVA, p>0.05. Error bars are 95% confidence intervals from Poisson model of 3 replicate measurements.

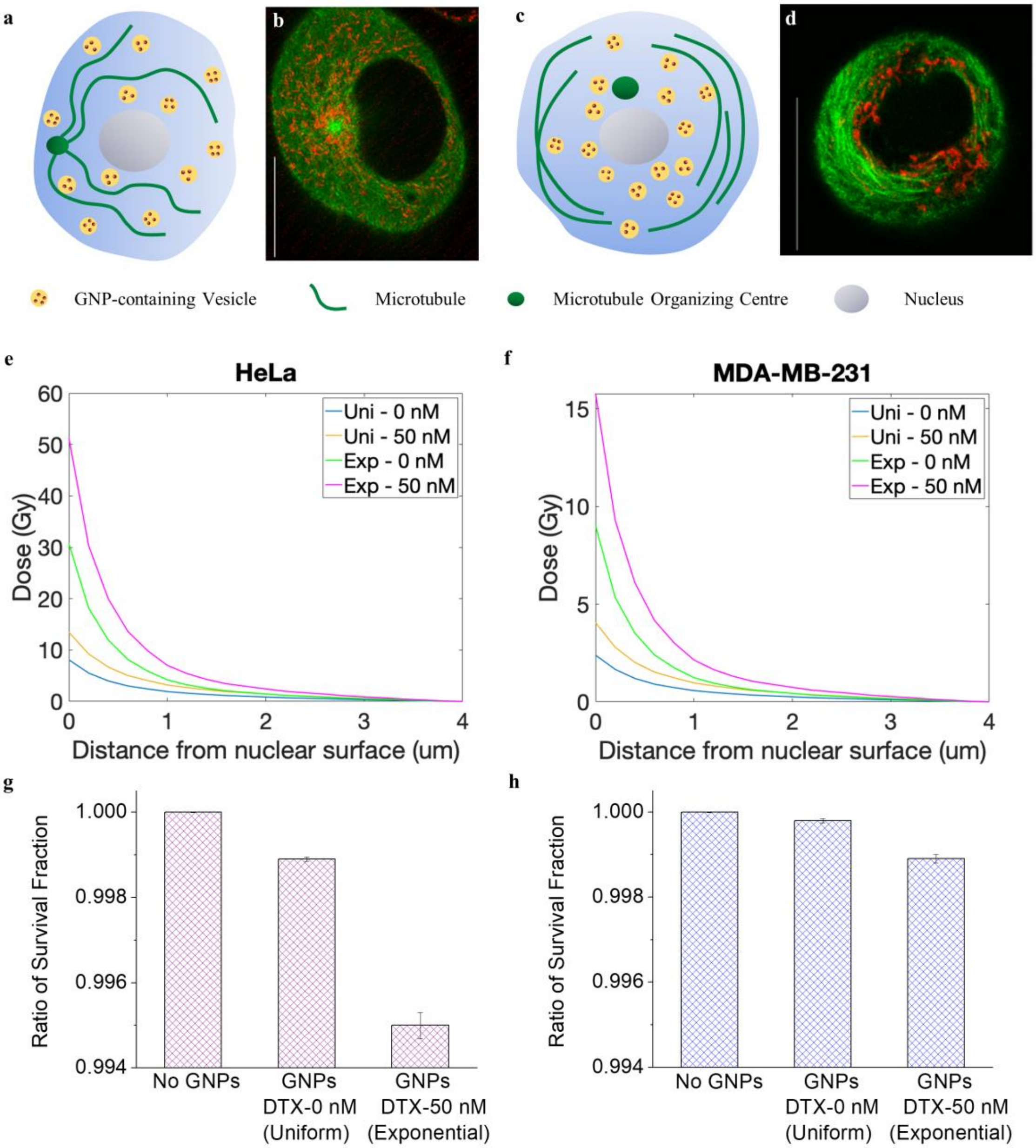

Figure 20: Monte Carlo simulations of GNP dose.

a, c) Schematic of GNP distribution in control (**a**) and DTX-treated (**c**) cells. Yellow circles represent vesicles containing red GNPs, and green represents microtubules. **b, d)** Confocal images of HeLa cells after vehicle control (**b**) or 50nM DTX (**c**). GNPs represented in red, MTs in green. **e, f)** Radial distribution of deposited dose inside the nucleus with GNP-containing vesicles uniformly (Uni) and exponentially (Exp) distributed in the cytoplasm. **g, h)** Relative survival fraction for described GNP distributions for irradiations of 2 Gy for HeLa (**g**) and MDA-MB-231 (**h**) cells.

3.7 Monte Carlo Simulation

Microdosimetric Monte Carlo simulations were performed to simulate the dose enhancement from a modified intracellular GNP distribution. Radial dose profiles of GNPs under irradiation from a clinical 6MV beam were calculated and superimposed over GNP locations in two model geometries:

1) Vesicles of GNPs distributed uniformly through the cytoplasm (see schematic **Figure 20a**). **Figure 20b** is an image of a control cell (not treated with DTX) showing the distribution of GNPs within the cell cytoplasm.

2) Vesicles distributed exponentially from the nucleus falling off radially (see schematic **Figure 20c**). This is a close representation of GNP distribution in cells treated with DTX as illustrated in **Figure 20d**.

Total numbers and uncertainties of GNPs per cell were taken from the uptake measurements in **Figure 14**. The dose was scored inside the nucleus (**Figure 20e, f**). GNPs caused significant dose enhancement, especially in the outer regions of the nucleus, with an increasing number of GNPs resulting in an increased dose enhancement. For example, 513,739 GNPs distributed exponentially with 50 nM docetaxel increased the radiation dose up to 50 Gy in the outer layer of the nucleus of HeLa cells. DTX with 50 nM concentrations induced a greater number of GNPs localized in close proximity to the nucleus. Therefore, a combined treatment of docetaxel, GNPs, and radiation was more effective to kill cancer cells compared to the one with radiation alone.

An adapted local effect model was introduced to predict survival fractions based on the experimental GNP uptake data (**Figure 20g, h**). It should be noted that our simulations do not take into account the effects of the treatment with DTX. The survival fraction is calculated only considering the additional cell kill induced by the presence of GNPs. The radiation response parameters (α and β) used in the calculations were the same as for the cells without DTX treatments. However, due to the expected synergistic effects of the two radiation sensitizers/enhancers, the difference in the observed biological effects between GNP and GNP+DTX in the experiments is expected to be higher than predicted by our simulation. It should further be noted that the simulations only consider the physical dose enhancement. Other effects, e.g. due to additionally created reactive oxygen species or GNP-induced cell stresses, are not modeled and result in a difference in the absolute scale of the effect between simulation and experiment. Nevertheless, the trends and relative differences consistently follow the simulation results.

Chapter 4: Conclusions

The transport processes that move cellular vesicles containing GNPs around are highly dependent on the microtubule (MT) network of the cell.[52] In a model random MT network, vesicle trapping behavior was observed near the nucleus.[102] These models do not fully cover the MT structural arrangements seen with DTX, however, they show that lengthening and randomly orienting MTs can have a significant effect on exocytosis and cause perinuclear localization of GNP-containing structures. We showed that cells treated with DTX retained GNPs very effectively closer to the peri-nuclear region. As discussed in the introduction, GNPs are being tested as radiation dose enhancers and having them closer to the nucleus could produce more radiation damage to cancer cells.[81] Further, DTX is typically given on a weekly basis when combined with radiotherapy as it remains in tumors longer than the rest of the body.[46, 89] This has an added advantage since it may also allow retention of GNPs during the fractionated radiotherapy treatment.

Finally, both GNPs and DTX are radiation sensitizers with different mechanisms of action and combined use of them is expected to produce synergistic effects in cancer radiotherapy. More than 50% of cancer patients receive radiation therapy as part of their treatment. Hence, we believe that understanding the uptake, distribution, and exocytosis of GNPs and its interaction with chemotherapy agents would lay the foundation for better and novel treatment approaches. GNPs are being successfully tested in phase I clinical trials.[103] We believe that our study will contribute to this effort and have a significant impact in future cancer therapy.

Chapter 5: Future Work

This work elucidates the mechanism of docetaxel's effect on intracellular GNP distribution, but further work remains to optimize this treatment for clinical use. The effects of varying DTX dosage and timing remain largely unexplored, though preliminary work suggests concurrent delivery with high DTX doses is most effective at causing increased uptake. However, DTX dosing is usually reduced when used with radiotherapy due to significant side effects.

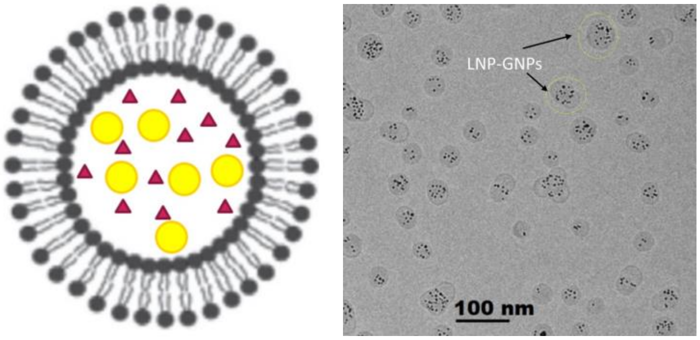

Figure 21: Proposed LNP system.

a) Lipid bilayer is represented in gray, GNPs in yellow, and DTX prodrug in red. **b)** TEM image of liposome-encapsulated GNPs.

One approach to mitigate the anticipated side effects with this combined treatment is to target both the gold nanoparticles and docetaxel to the tumour using a lipid nanoparticle carrier. Liposome nanoparticles (LNPs) are based on a lipid bilayer similar to a cell membrane that encloses an aqueous core, and can be passively targeted using the enhanced permeability and retention effect.[104] Our proposed system encapsulates both small GNPs and a docetaxel prodrug for uptake via receptor-mediated endocytosis, with activation of the prodrug occurring within the cell. The Chithrani lab is currently seeking funding in collaboration with the University of British Columbia, BC Cancer Agency, and Mayo Clinic to conduct *in vitro* and mouse model studies with this proposed LNP system.

References

1. Ruddon RW, MyiLibrary. Cancer biology. 4th ed. New York;Oxford;: Oxford University Press, 2007.
2. Ruddon RW. Cancer biology. 4th ed. New York;Oxford;: Oxford University Press, 2007.
3. Chabner B, Longo DL. Cancer chemotherapy and biotherapy: principles and practice. 5th ed. Philadelphia: Wolters Kluwer Health/Lippincott Williams & Wilkins, 2011.
4. Hall EJ, Willson S. Radiobiology for the Radiologist Seventh Edition2012.
5. Withrow S, Vail D, Page R. Withrow and MacEwen's small animal clinical oncology. Wiley Subscription Services, Inc; 2013. p. 319.
6. Boeckman HJ, Trego KS, Turchi JJ. Cisplatin sensitizes cancer cells to ionizing radiation via inhibition of nonhomologous end joining. Molecular cancer research : MCR. 2005;3(5):277-85.
7. Lawrence TS, Blackstock AW, McGinn C. The mechanism of action of radiosensitization of conventional chemotherapeutic agents. Seminars in Radiation Oncology. 2003;13(1):13-21.
8. Joiner M, Kogel Avd. Basic clinical radiobiology. Fifth ed. Boca Raton, FL: CRC Press/Taylor & Francis Group, 2019.
9. Meyers RA. Encyclopedia of molecular cell biology and molecular medicine. 2nd ed. Weinheim, Germany: Wiley-VCH, 2004.
10. Ciccia A, Elledge SJ. The DNA Damage Response: Making It Safe to Play with Knives. Molecular Cell. 2010;40(2):179-204.
11. Granger E, McNee G, Allan V, Woodman P. The role of the cytoskeleton and molecular motors in endosomal dynamics. Seminars in Cell & Developmental Biology. 2014;31:20-29.
12. Bridgewater RE, Norman JC, Caswell PT. Integrin trafficking at a glance. Journal of cell science. 2012;125(16):3695.
13. Snijder J, Reddy VS, May ER, Roos WH, Nemerow GR, Wuite GJL. Integrin and defensin modulate the mechanical properties of adenovirus. Journal of virology. 2013;87(5):2756--66.
14. Malumbres M, Barbacid M. Cell cycle, CDKs and cancer: a changing paradigm. Nature Reviews Cancer. 2009;9(3):153--66.
15. Delaney G, Jacob S, Featherstone C, Barton M. The role of radiotherapy in cancer treatment. Cancer. 2005;104(6):1129-37.
16. Chang DS, Lasley FD, Das IJ, Mendonca MS, Dynlacht JR. Basic Radiotherapy Physics and Biology. 2014 ed. Cham: Springer International Publishing, 2014.
17. Baskar R, Lee KA, Yeo R, Yeoh KW. Cancer and Radiation Therapy: Current Advances and Future Directions. INTERNATIONAL JOURNAL OF MEDICAL SCIENCES. 2012;9(3):193-99.
18. Teoh M, Clark CH, Wood K, Whitaker S, Nisbet A. Volumetric modulated arc therapy: a review of current literature and clinical use in practice. BRITISH JOURNAL OF RADIOLOGY. 2011;84(1007):967-96.

19. Iwamoto KS, Cochran ST, Winter J, Holburt E, Higashida RT, Norman A. Radiation dose enhancement therapy with iodine in rabbit VX-2 brain tumors. Radiotherapy and Oncology. 1987;8(2):161-70.

20. Matsudaira H, Ueno AM, Furuno I. Iodine Contrast Medium Sensitizes Cultured Mammalian Cells to X Rays but Not to γ Rays. Radiation Research. 1980;84(1):144-48.

21. Nath R, Bongiorni P, Rockwell S. Iododeoxyuridine Radiosensitization by Low- and High-Energy Photons for Brachytherapy Dose Rates. Radiation Research. 1990;124(3):249-58.

22. Wang AZaBVaVCCaGFaAFaZLaSMaYKaCMJaL. Superparamagnetic Iron Oxide Nanoparticle-Aptamer Bioconjugates for Combined Prostate Cancer Imaging and Therapy. ChemMedChem. 2008;3(9):1311--15.

23. Wang H, Mu X, He H, Zhang X-D. Cancer Radiosensitizers. Trends in Pharmacological Sciences. 2018;39(1):24-48.

24. Schuemann J, Berbeco R, Chithrani DB, Cho SH, Kumar R, McMahon SJ, et al. Roadmap to Clinical Use of Gold Nanoparticles for Radiation Sensitization. International Journal of Radiation Oncology Biology Physics. 2016;94(1):189--205.

25. Harrison E, Nicol JR, Macias–Montero M, Burke GA, Coulter JA, Meenan BJ, et al. A comparison of gold nanoparticle surface co-functionalization approaches using Polyethylene Glycol (PEG) and the effect on stability, non-specific protein adsorption and internalization. Materials Science and Engineering: C. 2016;62:710-18.

26. Su S, Zuo X, Pan D, Pei H, Wang L, Fan C, et al. Design and applications of gold nanoparticle conjugates by exploiting biomolecule–gold nanoparticle interactions. Nanoscale. 2013;5(7):2589-99.

27. Daraee H, Eatemadi A, Abbasi E, Fekri Aval S, Kouhi M, Akbarzadeh A. Application of gold nanoparticles in biomedical and drug delivery. Artificial Cells, Nanomedicine, and Biotechnology. 2016;44(1):410-22.

28. Cheng Y, Samia AC, Li J, Kenney ME, Resnick A, Burda C. Delivery and Efficacy of a Cancer Drug as a Function of the Bond to the Gold Nanoparticle Surface. Langmuir. 2010;26(4):2248-55.

29. Arai Y, Jee SY, Kim SM, Kwon Y, Jang W. Biomedical applications and safety issues of gold nanoparticles. Toxicology and Environmental Health Sciences. 2012;4(1):1--8.

30. Hainfeld JF, Slatkin DN, Smilowitz HM. The use of gold nanoparticles to enhance radiotherapy in mice. Physics in medicine and biology. 2004;49(18):N309.

31. Incerti S, Suerfu B, Xu J, Ivantchenko V, Mantero A, Brown JMC, et al. Simulation of Auger electron emission from nanometer-size gold targets using the Geant4 Monte Carlo simulation toolkit. Nuclear Instruments and Methods in Physics Research Section B: Beam Interactions with Materials and Atoms. 2016;372:91--101.

32. Sung W, Ye S-J, McNamara AL, McMahon SJ, Hainfeld J, Shin J, et al. Dependence of gold nanoparticle radiosensitization on cell geometry. Nanoscale. 2017;9(18):5843--53.

33. Her S, Jaffray DA, Allen C. Gold nanoparticles for applications in cancer radiotherapy: Mechanisms and recent advancements. Advanced Drug Delivery Reviews. 2017;109:84--101.

34. Lin Y, McMahon SJ, Scarpelli M, Paganetti H, Schuemann J. Comparing gold nano-particle enhanced radiotherapy with protons, megavoltage photons and kilovoltage photons: A Monte Carlo simulation. Physics in Medicine and Biology. 2014;59(24):7675--89.

35. Maeda H. The enhanced permeability and retention (EPR) effect in tumor vasculature: the key role of tumor-selective macromolecular drug targeting. Advances in Enzyme Regulation. 2001;41(1):189-207.

36. Liu C-J, Wang C-H, Chen S-T, Chen H-H, Leng W-H, Chien C-C, et al. Enhancement of cell radiation sensitivity by pegylated gold nanoparticles. Physics in Medicine \& Biology Chi-Jen Liu et al Phys Med Biol. 2010;55.

37. Cruje CaCBD. Integration of Peptides for Enhanced Uptake of PEGylayed Gold Nanoparticles. Journal of Nanoscience and Nanotechnology. 2015;15(3):2125--31.

38. Choy H. Taxanes in combined modality therapy for solid tumors. Critical Reviews in Oncology/Hematology. 2001;37(3):237-47.

39. Bellon JR, Lindsley KL, Ellis GK, Gralow JR, Livingston RB, Austin Seymour MM. Concurrent radiation therapy and paclitaxel or docetaxel chemotherapy in high-risk breast cancer. International Journal of Radiation Oncology • Biology • Physics. 2000;48(2):393-97.

40. Hennequin C, Giocanti N, Favaudon V. Interaction of ionizing radiation with paclitaxel (Taxol) and docetaxel (Taxotere) in HeLa and SQ20B cells. Cancer research. 1996;56(8):1842--50.

41. Mason KA, Hunter NR, Milas M, Abbruzzese JL, Milas L. Docetaxel enhances tumor radioresponse in vivo. Clinical Cancer Research. 1997;3(12):2431.

42. Ebrahimi Fard A, Tavakoli MB, Salehi H, Emami H. Synergetic effects of Docetaxel and ionizing radiation reduced cell viability on MCF-7 breast cancer cell. Applied Cancer Research. 2017;37(1):29.

43. Kumar P. A new paradigm for the treatment of high-risk prostate cancer: radiosensitization with docetaxel. Reviews in urology. 2003;5 Suppl 3(Suppl 3):S71-S77.

44. Fujii M, Tsukuda M, Satake B, Kubota A, Kida A, Kohno N, et al. Phase I/II trial of weekly docetaxel and concomitant radiotherapy for squamous cell carcinoma of the head and neck. International Journal of Clinical Oncology. 2004;9(2):107--12.

45. Barnadas A, Mesía R, Majem M, Galiana R, López-Pousa A, de Vega JM, et al. Phase I/II docetaxel plus concurrent hyperfractionated radiotherapy in locally advanced unresectable head and neck cancer (TAX.ES1.102 study). Clinical and Translational Oncology. 2011;13(4):254--60.

46. Kim ES, Khuri FR. Docetaxel and Radiation as Combined-Modality Therapy. 2002.

47. Bellon JR, Lindsley KL, Ellis GK, Gralow JR, Livingston RB, Seymour MMA. Concurrent radiation therapy and paclitaxel or docetaxel chemotherapy in high-risk breast cancer. International Journal of Radiation Oncology*Biology*Physics. 2000;48(2):393--97.

48. Brackstone M, Palma D, Tuck AB, Scott L, Potvin K, Vandenberg T, et al. Concurrent Neoadjuvant Chemotherapy and Radiation Therapy in Locally Advanced

Breast Cancer. International Journal of Radiation Oncology • Biology • Physics. 2017;99(4):769-76.

49. Snyder JP, Nettles JH, Cornett B, Downing KH, Nogales E. The binding conformation of Taxol in beta-tubulin: a model based on electron crystallographic density. Proceedings of the National Academy of Sciences of the United States of America. 2001;98(9):5312--6.

50. De Brabander M, Geuens G, Nuydens R, Willebrords R, De Mey J. Taxol induces the assembly of free microtubules in living cells and blocks the organizing capacity of the centrosomes and kinetochores. Proc Natl Acad Sci U S A. 1981;78(9):5608-612.

51. Paoletti A, Giocanti N, Favaudon V, Bornens M. Pulse treatment of interphasic HeLa cells with nanomolar doses of docetaxel affects centrosome organization and leads to catastrophic exit of mitosis. JOURNAL OF CELL SCIENCE. 1997;110:2403-15.

52. Granger E, McNee G, Allan V, Woodman P. The role of the cytoskeleton and molecular motors in endosomal dynamics. Seminars in Cell & Developmental Biology. 2014;31:20--29.

53. Anselmo AC, Mitragotri S. A Review of Clinical Translation of Inorganic Nanoparticles. The AAPS Journal. 2015;17(5):1041-54.

54. Cui L, Her S, Borst GR, Bristow RG, Jaffray DA, Allen C. Radiosensitization by gold nanoparticles: Will they ever make it to the clinic? Radiotherapy and Oncology. 2017;124(3):344-56.

55. Sharifi M, Attar F, Saboury AA, Akhtari K, Hooshmand N, Hasan A, et al. Plasmonic gold nanoparticles: Optical manipulation, imaging, drug delivery and therapy. Journal of Controlled Release. 2019;311-312:170-89.

56. Cui L, Her S, Dunne M, Borst GR, De Souza R, Bristow RG, et al. Significant Radiation Enhancement Effects by Gold Nanoparticles in Combination with Cisplatin in Triple Negative Breast Cancer Cells and Tumor Xenografts. Radiation research. 2017;187(2):147-60.

57. Park J, Park J, Ju EJ, Park SS, Choi J, Lee JH, et al. Multifunctional hollow gold nanoparticles designed for triple combination therapy and CT imaging. Journal of Controlled Release. 2015;207:77-85.

58. Li T, Zhang M, Wang J, Wang T, Yao Y, Zhang X, et al. Thermosensitive Hydrogel Co-loaded with Gold Nanoparticles and Doxorubicin for Effective Chemoradiotherapy. The AAPS Journal. 2016;18(1):146-55.

59. Yang CaUJaCD. Colloidal Gold-Mediated Delivery of Bleomycin for Improved Outcome in Chemotherapy. Nanomaterials. 2016;6(3):48.

60. Yang C. Combined Cancer Therapy Using Gold Nanoparticles. 2018.

61. Yang C, Bromma K, Sung W, Schuemann J, Chithrani D. Determining the Radiation Enhancement Effects of Gold Nanoparticles in Cells in a Combined Treatment with Cisplatin and Radiation at Therapeutic Megavoltage Energies. Cancers. 2018;10(5):150.

62. Fathy MM, Mohamed FS, Elbialy N, Elshemey WM. Multifunctional Chitosan-Capped Gold Nanoparticles for enhanced cancer chemo-radiotherapy: An invitro study. Physica Medica. 2018;48:76-83.

63. Kim K, Oh KS, Park DY, Lee JY, Lee BS, Kim IS, et al. Doxorubicin/gold-loaded core/shell nanoparticles for combination therapy to treat cancer through the enhanced tumor targeting. Journal of Controlled Release. 2016;228:141-49.

64. Werner MEaCJAaKSaCNDaSRaLCaNMEaCRCa. Folate-Targeted Polymeric Nanoparticle Formulation of Docetaxel Is an Effective Molecularly Targeted Radiosensitizer with Efficacy Dependent on the Timing of Radiotherapy. ACS Nano. 2011;5(11):8990--98.

65. Ernsting MJaTW-LaMNWaLS-D. Preclinical pharmacokinetic, biodistribution, and anti-cancer efficacy studies of a docetaxel-carboxymethylcellulose nanoparticle in mouse models. Biomaterials. 2012;33(5):1445--54.

66. Sethi MaSRaKSaWMEaWECaMDTaKSRaZLaW. Effect of drug release kinetics on nanoparticle therapeutic efficacy and toxicity. Nanoscale. 2014;6(4):2321--27.

67. Ramanlal Chaudhari K, Kumar A, Megraj Khandelwal VK, Ukawala M, Manjappa AS, Mishra AK, et al. Bone metastasis targeting: A novel approach to reach bone using Zoledronate anchored PLGA nanoparticle as carrier system loaded with Docetaxel. Journal of Controlled Release. 2012;158(3):470-78.

68. Wang ECaSRaWMEaSMaWAWaWAZ. Differential cell responses to nanoparticle docetaxel and small molecule docetaxel at a sub-therapeutic dose range. Nanomedicine: Nanotechnology, Biology and Medicine. 2014;10(2):321--28.

69. Feng S-S, Mei L, Anitha P, Gan CW, Zhou W. Poly(lactide)–vitamin E derivative/montmorillonite nanoparticle formulations for the oral delivery of Docetaxel. Biomaterials. 2009;30(19):3297-306.

70. François A, Laroche A, Pinaud N, Salmon L, Ruiz J, Robert J, et al. Encapsulation of Docetaxel into PEGylated Gold Nanoparticles for Vectorization to Cancer Cells. ChemMedChem. 2011;6(11):2003-08.

71. de Oliveira R, Zhao P, Li N, de Santa Maria LC, Vergnaud J, Ruiz J, et al. Synthesis and in vitro studies of gold nanoparticles loaded with docetaxel. International Journal of Pharmaceutics. 2013;454(2):703-11.

72. Thambiraj S, Shruthi S, Vijayalakshmi R, Ravi Shankaran D. Evaluation of cytotoxic activity of docetaxel loaded gold nanoparticles for lung cancer drug delivery. Cancer Treatment and Research Communications. 2019;21:100157.

73. Li C, Li D, Wan G, Xu J, Hou W. Facile synthesis of concentrated gold nanoparticles with low size-distribution in water: temperature and pH controls. Nanoscale Research Letters. 2011;6(1):1-10.

74. Haiss W, Thanh NTK, Aveyard J, Fernig DG. Determination of size and concentration of gold nanoparticles from UV-Vis spectra. ANALYTICAL CHEMISTRY. 2007;79(11):4215-21.

75. Hafner M, Niepel M, Chung M, Sorger PK. Growth rate inhibition metrics correct for confounders in measuring sensitivity to cancer drugs. Nature methods. 2016;13(6):521-7.

76. Stoeva SIP, B.L.V.; Uma, Sitharaman; Stoimenov, Peter K.; Zaikovski, Vladimir; Sorensen, Christopher M.; Klabunde, Kenneth J. Face-Centered Cubic and Hexagonal Closed-Packed Nanocrystal Superlattices of Gold Nanoparticles Prepared by Different Methods. J PHys Chem B. 2003;107:7441-48.

77. Brasselman H. CFAssay: Statistical analysis for the Colony Formation Assay.

78. Braselmann H, Michna A, Heß J, Unger K. CFAssay: statistical analysis of the colony formation assay. Radiation oncology (London, England). 2015;10:223-23.

79. Perl J, Shin J, Schmann J, Faddegon B, Paganetti H. TOPAS: An innovative proton Monte Carlo platform for research and clinical applications. Medical Physics. 2012;39(11):6818--37.

80. Schuemann J, McNamara AL, Ramos-Mndez J, Perl J, Held KD, Paganetti H, et al. TOPAS-nBio: An Extension to the TOPAS Simulation Toolkit for Cellular and Sub-cellular Radiobiology. Radiation Research. 2018;191(2):125.

81. Lin Y, McMahon SJ, Paganetti H, Schuemann J. Biological modeling of gold nanoparticle enhanced radiotherapy for proton therapy. Physics in Medicine and Biology. 2015;60(10):4149--68.

82. Rieck K, Bromma K, Sung W, Bannister A, Schuemann J, Chithrani DB. Modulation of gold nanoparticle mediated radiation dose enhancement through synchronization of breast tumor cell population. The British Journal of Radiology. 2019;92(1100):20190283.

83. Jain S, Coulter JA, Hounsell AR, Butterworth KT, Mcmahon SJ, Hyland WB, et al. Cell-Specific Radiosensitization by Gold Nanoparticles at Megavoltage Radiation Energies. 2011.

84. Yang C, Bromma K, Chithrani D. Peptide mediated in vivo tumor targeting of nanoparticles through optimization in single and multilayer in vitro cell models. Cancers. 2018;10(3):1--3.

85. Cruje C, Chithrani DB. Polyethylene Glycol Functionalized Nanoparticles for Improved Cancer Treatment. Reviews in Nanoscience and Nanotechnology. 2014;3(1):20-30.

86. Bromma K, Rieck K, Kulkarni J, O'Sullivan C, Sung W, Cullis P, et al. Use of a lipid nanoparticle system as a Trojan horse in delivery of gold nanoparticles to human breast cancer cells for improved outcomes in radiation therapy. Cancer Nanotechnology. 2019;10(1):1.

87. Wohl AR, Michel AR, Kalscheuer S, Macosko CW, Panyam J, Hoye TR. Silicate esters of paclitaxel and docetaxel: Synthesis, hydrophobicity, hydrolytic stability, cytotoxicity, and prodrug potential. Journal of Medicinal Chemistry. 2014;57(6):2368--79.

88. de Oliveira R, Pengxiang Z, Na L, de Santa Maria LC, Vergnaud J, Ruiz J, et al. Synthesis and in vitro studies of gold nanoparticles loaded with docetaxel. International Journal of Pharmaceutics. 2013;454(2):703--11.

89. Clarke SJ, Rivory LP. Clinical Pharmacokinetics of Docetaxel. Clinical Pharmacokinetics. 1999;36(2):99--114.

90. Hainsworth JD. Practical aspects of weekly docetaxel administration schedules. The oncologist. 2004;9(5):538--45.

91. Hernández-Vargas H, Palacios J, Moreno-Bueno G. Molecular profiling of docetaxel cytotoxicity in breast cancer cells: Uncoupling of aberrant mitosis and apoptosis. Oncogene. 2007;26(20):2902--13.

92. Miyanaga S, Ninomiya, I., Tsukada, T., Okamoto, K., Harada, S., Nakanuma, S., Sakai, S., Makino, I., Kinoshita, J., Hayashi, H., Nakamura, K., Oyama, K., Nakagawara, H., Miyashita, T., Tajima, H., Takamura, H., Fushida, S., Ohta, T. Concentration-

dependent radiosensitizing effect of docetaxel in esophageal squamous cell carcinoma cells. International Journal of Oncology. 2016;48:517-24.

93. Morse DL, Gray H, Payne CM, Gillies RJ. Docetaxel induces cell death through mitotic catastrophe in human breast cancer cells. Molecular cancer therapeutics. 2005;4(10):1495--504.

94. Hainfeld JF, Slatkin DN, Smilowitz HM. The use of gold nanoparticles to enhance radiotherapy in mice. Physics in Medicine and Biology. 2004;49(18):N309--N15.

95. Chithrani BD, Chan WCW. Elucidating the mechanism of cellular uptake and removal of protein-coated gold nanoparticles of different sizes and shapes. Nano Letters. 2007;7(6):1542--50.

96. Chithrani DB. Intracellular uptake, transport, and processing of gold nanostructures. Molecular Membrane Biology. 2010;27(7):299--311.

97. De Franceschi N, Hamidi H, Alanko J, Sahgal P, Ivaska J. Integrin traffic - the update. Journal of cell science. 2015;128(5):839-52.

98. Bridgewater RE, Norman JC, Caswell PT. Integrin trafficking at a glance. Journal of Cell Science. 2012;(125):3695--701.

99. Kim JA, Aberg C, Salvati A, Dawson KA. Role of cell cycle on the cellular uptake and dilution of nanoparticles in a cell population. Nature Nanotechnology. 2012;7(1):62--68.

100. Miyanaga S, Ninomiya I, Tsukada T, Okamoto K, Harada S, Nakanuma S, et al. Concentration-dependent radiosensitizing effect of docetaxel in esophageal squamous cell carcinoma cells. International Journal of Oncology. 2016;48(2):517--24.

101. Paoletti A, Giocanti N, Favaudon V, Bornens M. Pulse treatment of interphasic HeLa cells with nanomolar doses of docetaxel affects centrosome organization and leads to catastrophic exit of mitosis. Journal of cell science. 1997;110 (Pt 19):2403-15.

102. Ando D, Korabel N, Huang KC, Gopinathan A. Cytoskeletal Network Morphology Regulates Intracellular Transport Dynamics. Biophysical Journal. 2015;109(8):1574--82.

103. Paciotti GF, Myer L, Weinreich D, Goia D, Pavel N, McLaughlin RE, et al. Colloidal gold: a novel nanoparticle vector for tumor directed drug delivery. Drug delivery. 2004;11(3):169-83.

104. Allen TM, Cullis PR. Liposomal drug delivery systems: From concept to clinical applications. Advanced Drug Delivery Reviews. 2013;65(1):36-48.

Appendix 1: Additional Images

Appendix 1.1: Confocal Z-stacks of HeLa cells. **a**) Vehicle control treated. **b**) (next page) 50nM DTX-treated. GNPs are shown in red and MTs are shown in green. The last image in each set is a confocal slice showing the nuclei in blue. The scale bar is 25 µm. Slices are separated by 0.4µm.

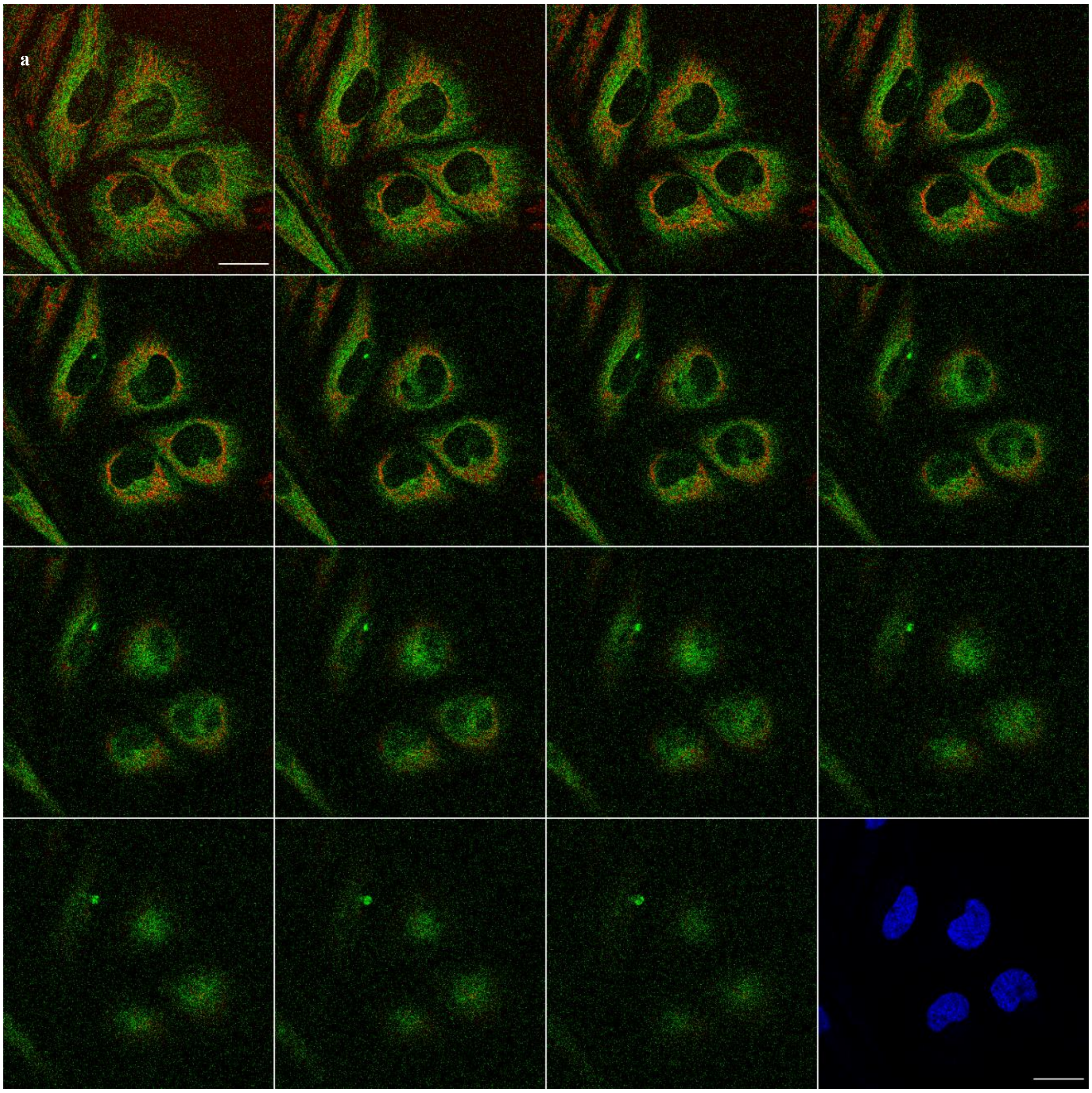

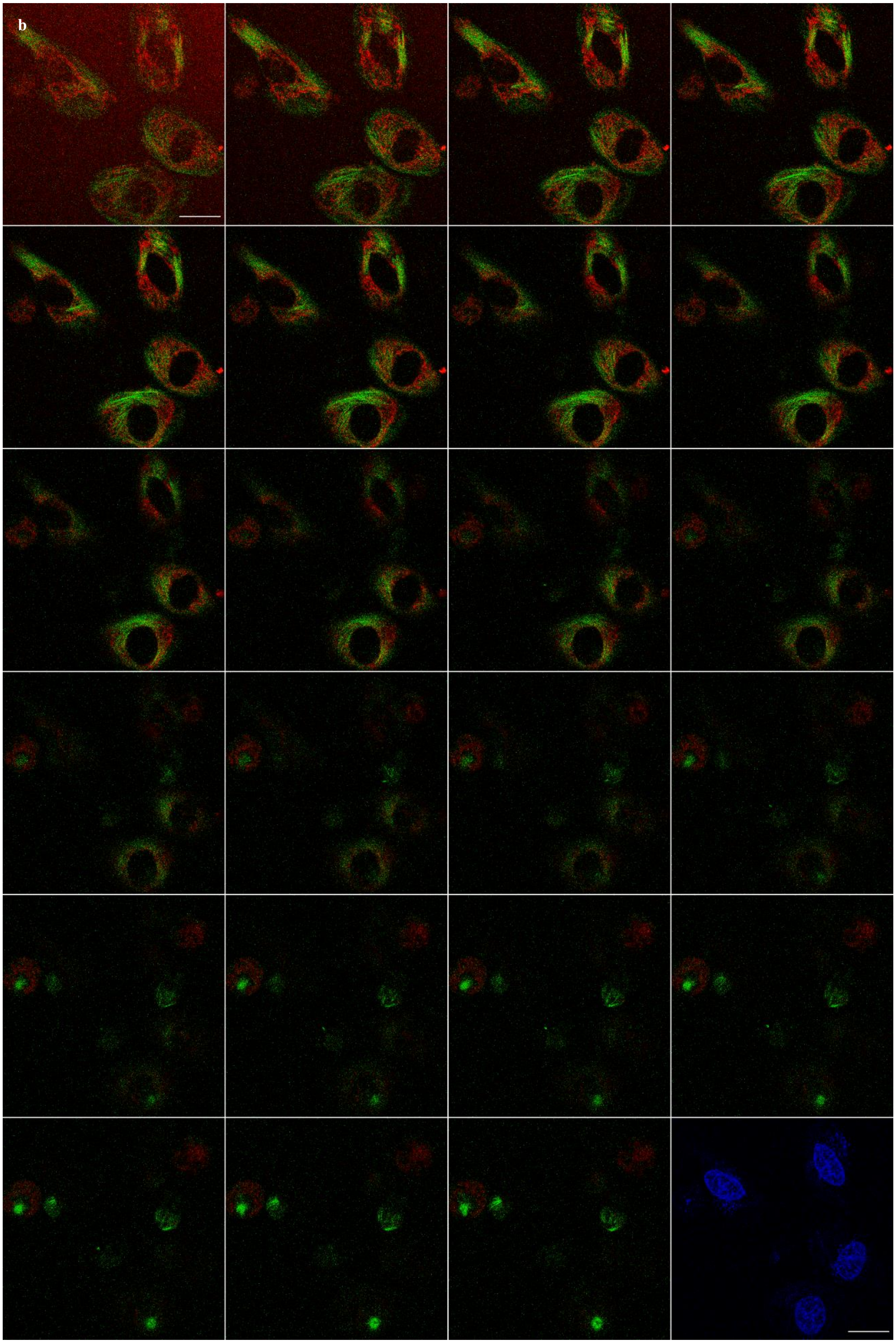
b

Appendix 1.2: Variations of Docetaxel's effect on GNP localization. Optical images of distribution of GNPs and MTs in HeLa (**a-b**) and MDA-MB-231 (**c**) cells treated with 50nM DTX for 24h. **a** and **c** show GNP aggregation at the ends of linear MT bundles. **b** shows collection near the nucleus and in a region with a lower MT density. The scale bar is 25 µm. GNPs are shown in red and MTs are shown in green. The scale bar is 25 µm.